Metamorphic reactions and their implication for the fluid budget in metapelites at seismogenic depths in subduction zones

Kristijan Rajič, Hugues Raimbourg, Catherine Lerouge, Vincent Famin, Benoît Dubacq, Aurélien Canizarés, Ida Di Carlo, Nicolas Maubec

Metamorphic reactions and their implication for the fluid budget in metapelites at seismogenic depths in subduction zones

Kristijan Rajič[1], Hugues Raimbourg[1], Catherine Lerouge[2], Vincent Famin[3,4], Benoit Dubacq[5], Aurélien Canizarés[6], Ida Di Carlo[1], Nicolas Maubec[2]

[1] Institut des Sciences de la Terre d'Orléans, Université d'Orléans/CNRS/BRGM UMR7327, 1A Rue de la Férollerie, 45100 Orléans, France

[2] B.R.G.M., BP 6009, 45060 Orléans cedex 2, France

[3] Université de La Réunion, Laboratoire GéoSciences Réunion, F-97744 Saint-Denis, France

[4] Université de Paris, Institut de Physique du Globe de Paris, CNRS, UMR 7154, F-75005 Paris, France

[5] Institut des Sciences de la Terre de Paris (ISTeP), UMR 7193, CNRS-INSU, Sorbonne Université, 75005 Paris, France

[6] CNRS, CEMHTI UPR3079, Univ. Orléans, F-45071 Orléans, France

Abstract

In order to determine fluid-mineral reactions and the fluid budget in subduction zones, we have examined rocks from two accretionary complexes, the Kodiak (Alaska) and Shimanto (Japan), that were buried at the temperature conditions of the seismogenic zone. Maximum burial temperatures based on Raman spectroscopy of carbonaceous material in both examples range from 230 to 350°C, whereas pressures reached up to ~3 and ~4kbars (based on multi-equilibrium modelling) in the higher-grade units of the Japanese and Alaskan complexes, respectively. At 230-260°C, chlorite is interpreted as a coproduct of the lower-grade smectite-to-illite transformation. Chlorite content increases as temperature increases to 330-350°C, as a result of illite-to-chlorite transformation. Other reactions include pyrite oxidation, dissolution of titanite and precipitation of anatase. Whole-rock chemistry points to the absence of systematic chemical variations in the temperature range between 250 and 350°C and only local transport of quartz and albite from the matrix, to veins nearby, is observed. Qualitative analyses of the composition of fluid inclusions using decrepitation method show that the composition of the fluid is significantly different from the original seawater trapped in pores. In addition, the salinity of fluid inclusions in the quartz veins at 230-260°C, analyzed using the Raman spectrum of water, is lower than seawater and interpreted as dilution of the original seawater by the fresh water released by the smectite-to-illite transformation. In

contrast, veins formed at 330-350°C contain fluid inclusions with a salinity on the order of or higher than that of seawater. The increase in salinity for temperatures of 250-350°C reflects hydration reactions, which are mostly controlled by chlorite crystallization. This study demonstrates an uptake of pore fluid by mineral reactions at temperature corresponding to the base of the seismogenic zone, which is in contrast to the general trend of dehydration reactions occurring along rock burial in subduction zones.

1. Introduction

Fluids are heavily involved in the majority of subduction zone processes. For instance, the presence of pore fluids highly impacts the rheological behavior of subducted lithologies (e.g., Fagereng et al., 2018; Hacker et al., 2003; Muñoz-Montecinos, Angiboust, & Garcia-Casco, 2021), and influences seismic activity via pore fluid pressure variations (Audet & Schwartz, 2013; Davis et al., 1983; Saffer & Tobin, 2011). Dehydration reactions in deeply subducted lithologies are also responsible for the generation of arc magmas due to the melting action of volatile species of the mantle (Bebout, 1991; Elliott, 2003; Hacker, 2008; Stern, 2011). Because fluids are reactants or products of metamorphic reactions, their abundance, nature and chemistry change with burial. Beyond the drilling reach of ODP/IODP programs (<5 km), our knowledge of fluid composition mostly relies on studies of fluid inclusions and mineral transformations in rocks from exhumed subducted complexes (e.g., Agard et al., 2000; Herviou et al., 2021; Raimbourg et al., 2018; Scambelluri et al., 2015). In veins that have trapped deep fluids as fluid inclusions, the most commonly retrieved property is salinity, converted to NaCl equivalent with the assumption that NaCl is the dominant species (Agard et al., 2000; Brantley & Fisher, 1997; Herviou et al., 2021; Kondo et al., 2005; Nishiyama et al., 2021; Raimbourg, 2015, 2018; Rossetti et al., 2006; Rowe et al., 2009; Sadofsky & Bebout, 2004). However, few studies have actually analyzed the chemistry of the occluded fluid (e.g., Scambelluri et al., 2004, 2015; Yoshida et al., 2015).

Sediments are the major carriers of fluids (mostly water) into subduction zones (Jarrard, 2003; Plank, 2014; Stern, 2002), together with the altered and serpentinized oceanic lithosphere (Peacock, 1993; Schmidt & Poli, 2014; Reynard, 2013; Rupke, 2004). Average seafloor shales contain up to 70 vol.% of pore fluids that are chemically similar to sea water, and about 7 wt.% as crystal-bound H_2O (Plank, 2014). During burial, most of the interstitial water is expelled from sediments at shallow depths by compaction and cementation processes; leaving only <10 vol.% in pore spaces (Fagereng et al., 2018; Kastner et al., 2014; Kominz & Pekar, 2001; Saffer & Tobin, 2011). Following pore collapse, the occurrence of prograde metamorphic reactions controls the water budget (Rupke, 2004; Schmidt & Poli, 2014). The smectite-to-illite transformation occurs in the temperature range 60-150°C and releases significant amount of H_2O

that is bounded in minerals, thus, it reduces the salinity of pore fluids (e.g., Kastner et al., 2014; Saffer et al., 2012). Upon further burial, several important dehydration reactions have been reported above 400°C, such as carpholite and chlorite breakdown in the blueschist facies or the glaucophane, as well as lawsonite and chlorite breakdown in the eclogite facies (Agard et al., 2001; Angiboust & Agard, 2010; Bebout, 1991; Bebout et al., 2013; Becker et al., 2000; van Keken et al., 2002; Lefeuvre et al., 2020; Muñoz-Montecinos et al., 2021; Peacock, 1993; Simons et al., 2010; Spandler et al., 2003). Beside dehydration reactions, other mineral transformations may strongly impact to the chemical composition of fluids, such as the transformation of biotite into chlorite, which is correlated to the transition of CH_4-dominated to CO_2-dominated fluids (Dubessy et al., 1983; Ferry, 1981; Hall, 1986; Tarantola et al., 2007, 2009).

Only few metamorphic reactions have been identified in subducted sediments in the range 150-350°C, such as the formation of lawsonite and Mg-Fe carpholite (Goffé & Chopin, 1986; Lefeuvre et al., 2020). Many exhumed sub-greenschist and greenschist facies rocks (peak-metamorphism at 150-350°C) contain evidence of ancient fluid pathways in form of metamorphic veins, such as the Kodiak accretionary prism in Alaska (Brantley & Fisher, 1997; Fisher et al., 1995; Fisher & Brantley, 2014; Vrolijk et al., 1988), the Shimanto Belt in Japan (Nishiyama et al., 2021; Raimbourg et al., 2015, 2018), the Franciscan Complex in California, or the Otago Schists in New Zealand (Breeding & Ague, 2002; Fagereng et al., 2011). However, the mineral reactions and the influence of reactions on the pore fluid budget is relatively poorly documented compared to deeper metamorphism (e.g., Fagereng & Cooper, 2010; Frey, 1978; Kameda et al., 2011a; Rahn et al., 1994; Raimbourg et al., 2009; Schmidt et al., 1997; Wang, 1996).

The objective of this study is to fill this knowledge gap, by describing the prograde evolution of mineral assemblages, the scale of chemical transport and the fluid budget in sediments subducted and buried down to greenschist facies. To do so, we targeted two accretionary prisms: Kodiak and the Shimanto Belt, because the peak-metamorphic conditions are well preserved and constrained to 200-350°C at both localities (Brantley & Fisher, 1997; Palazzin et al., 2016; Raimbourg et al., 2014, 2021; Rowe et al., 2009; Vrolijk et al., 1988). First, we studied changes in microstructures, mineralogy and whole-rock chemistry with increasing temperature. Mineral chemistry was then used to test the mineral equilibrium for possible estimations of the pressure-temperature conditions based on multi-phase equilibrium model (Dubacq et al., 2010; Vidal et al., 2006). Finally, we studied fluid inclusions as fluid witnesses of the deep metamorphic reactions. Based on these results, we propose several mineral reactions and evaluate fluid-rock interactions, as well as changes in the salinity among subduction-related fluids from the two paleo-

accretionary complexes. Our results are of importance for quantifying the fluid budget of sediments undergoing burial in the greenschist facies realm during subduction.

2. Geological settings and sampling strategy

We sampled metapelites and adjacent veins along various units of the two selected accretionary prisms (Fig. 1; Palazzin et al., 2016; Raimbourg et al., 2021) to investigate the dependence of fluid-mineral reactions on peak-metamorphic temperature and pressure. The list of samples and their peak-metamorphic conditions is presented in Table 1.

2.1. Kodiak accretionary complex

Kodiak is a paleo-accretionary complex exposed in Kodiak archipelago, southern Alaska, which consists of coherent slices of metasediments and tectonic mélanges (Fig. 1a) that decrease in age towards the modern trench (Byrne & Fisher, 1987; Connelly, 1978; Moore et al., 1983; Plafker et al., 1994). The Kodiak accretionary complex is classically divided into several trench-parallel units (Fig. 1a). The Late Cretaceous Kodiak Formation consists of deep trench sediments. The formation is subdivided into three belts (Landward, Central and Seaward Belts), which are also characterized by the peak-metamorphic temperature and structural fabric variations (Brantley & Fisher, 1997; Rowe et al., 2009; Sample & Fisher, 1986; Vrolijk et al., 1988). The Kodiak Landward Belt (KLB) in Uyak Bay consists of intercalated sandstone/siltstone and mudstone beds (Fig. 2a), with occasionally disrupted strata closer to its northern boundary marked by the Uganik Thrust (Fisher & Byrne, 1987; Rowe et al., 2009). The veins from Landward Belt are Mode 1 (Mode 1 veins refer to mineralized fractures characterized by the opening direction perpendicular to the fracture plane; Bons et al., 2012) quartz-calcite veins oriented almost perpendicular to the bedding stratification (Fig. 2a) and are interpreted as forming in the sediments during underthrusting, where the maximum compressive stress (σ_1) is in sub-vertical position (Byrne & Fisher, 1990; Fisher & Byrne, 1990). The temperatures derived from fluid inclusions in Mode 1 quartz veins are in the range of 215-255°C for the Landward Belt at Raspberry and Afognak islands (Vrolijk et al., 1988). The Kodiak Central Belt (KCB), investigated in Seal Bay, is characterized by a sub-horizontal bedding stratification and foliation (S_1), with top-to-the-trench shear bands and recumbent folds (Raimbourg et al., 2021; Sample & Fisher, 1986; Sample & Moore, 1987). In Seal Bay, two types of veins have been observed: Shear veins at low angle to the foliation with a fibrous structure parallel to the stretching direction on foliation plane, and Mode 1 quartz veins, often in form of en échelon arrays (Fig. 2c). En

120 échelon veins cut across the foliation but are folded perpendicular to the foliation and are interpreted as
121 formed at peak metamorphic conditions (Fisher & Brantley, 2014; Raimbourg et al., 2021). The Central
122 Belt experienced the highest metamorphic conditions of the Kodiak Formation, reaching temperatures of
123 ~330°C as determined from Raman spectroscopy of carbonaceous material (RSCM; Raimbourg et al.,
124 2021). Towards the southeast, the Kodiak Seaward Belt (KSB) is characterized by intercalated sandstone
125 and shale layers. This belt experienced horizontal noncoaxial shortening with top-to-the-SE thrust faults
126 (Sample & Moore, 1987). Vitrinite reflectance in the Kodiak Formation has an average value of 3.73 and
127 corresponds to a temperature of ~225°C (Sample & Moore, 1987).

128 **2.2. Shimanto Belt, Japan**

129 The Shimanto Belt is a paleo-accretionary wedge (Taira, 1988) exposed on the islands of Honshu, Kyushu
130 and Shikoku in Japan. It is composed of several parallel units elongated SW-NE and stacked from the NW
131 to the SE, this general trend is consistent with the active Nankai Trough (Fig. 1b). The Shimanto Belt in
132 Kyushu is also divided into several units, among which two are selected for this study, the Foliated
133 Morotsuka and the Hyuga Tectonic Mélange.
134 The Foliated Morotsuka (FM) is composed of sheared and strongly foliated lithologies, including deep-sea
135 sediments and basaltic lenses embedded within a metapelitic matrix. The age of the sediments range from
136 the Cenomanian to the Turonian (Saito et al., 1996). A strong metamorphic foliation is present, along with
137 a N-S and NNW-SSE stretching lineation (Raimbourg et al., 2009, 2014; Ujiie et al., 2018). The Foliated
138 Morotsuka is separated from the Hyuga Group by the Nobeoka Tectonic Line (NTL; Teraoka & Okumura,
139 1992), an out-of-sequence thrust (Kondo et al., 2005). Based on metamorphic assemblages in basaltic
140 lenses, the pressure-temperature conditions in the FM were estimated to be 3-5 kbar and 300-350°C
141 (Toriumi & Teruya, 1988). RSCM yielded a maximum temperature of 345 ± 30°C for the FM (Palazzin et
142 al., 2016). Similarly to the veins from the KCB, the examined veins from the FM are Mode 1 fractures often
143 arranged as en échelon arrays (Fig. 2d), cutting across the foliation and shortened perpendicular to the
144 foliation (Raimbourg et al., 2021).
145 The Hyuga Group is divided into Hyuga Tectonic Mélange (HTM) and Coherent Hyuga. In this study the
146 Hyuga Tectonic Mélange is examined, which consists of strongly sheared sandstone lenses embedded in
147 a pelitic matrix. Based on microfossil assemblages, the sedimentation age is from the Middle Eocene to
148 the Early Oligocene (Nishi, 1988; Sakai et al., 1984)**.** Based on RSCM, the peak-temperature of deformation
149 was estimated to ~245 ± 30°C (Palazzin et al., 2016). The dominant veins in the HTM are Mode 1 quartz-

filled extension fractures oriented perpendicular to the NW-SE stretching direction of sandstone lenses (Fig. 2b; Raimbourg et al., 2014).

3. Analytical methods

3.1. Whole-rock chemistry

Samples for major element whole-rock analysis were crushed after removing any visible macro- and micro-veins in order to estimate the chemical composition of the pelitic matrix. Major elements were analyzed by X-ray fluorescence (XRF) at ALS lab (Loughrea Galway, Ireland; analytical code ME_XRF26). To prepare glass beads, crushed samples (~0.5 g) were fused using a platinum mold into a fusion disk and mixed with lithium metaborate as a flux. The disks were then analyzed by XRF, where the concentrations of major elements (oxides) were determined in conjunction with loss-on-ignition (LOI) at 1000°C. Analyzed elements and parameters are Si, Ti, Al, Cr, Fe, Mn, Mg, Ca, Na, K, P, S, Sr, Ba and LOI. Elements were calibrated in oxide weight percentage form.

3.2. X-Ray Diffraction

X-ray diffraction (XRD) measurements were carried at BRGM, Orléans, France, using a BRUKER D8 Advance X-ray diffractometer equipped with a Cu Kα radiation ($\lambda\ k_\alpha$ = 0.15406 nm) operating at 40 kV and 40 mA. X-Ray diffraction on bulk-powder was used for a first-order estimation of the mineralogy, including the nature of phyllosilicates. Samples were micronized in ethanol using an XRD Mill McCrone (Retsch), dried at 40°C and homogenized. XRD patterns were recorded on randomly oriented powder samples from 4 to 90°2θ, with a step of 0.03°2θ and a step time of 480 seconds. Quantitative analyses of X-ray diffractograms were carried out using the SiroQuant™ program, version 4 (Taylor & Clapp, 1991).

The <2 µm fraction was then isolated from the bulk samples. To do so, the crushed powder was firstly treated with acetate (pH = 5.0) to dissolve carbonates, secondly with 0.01 M $CaCl_2$ to saturate interlayer space of clay minerals if present, and finally washed with pure water. Then clay particles were dispersed by ultrasonics in deionised water and the suspension was left to rest 100 minutes. Then <2 µm fraction was isolated by sampling the upper part of the suspension and deposited on a thin section. X-ray diffraction patterns were acquired firstly on the oriented deposit dried at 50°C, then saturated with ethylene glycol under vapor tension at 60°C for at least 16 hours, to identify the clay mineral varieties. XRD patterns were recorded on oriented deposits from 2 to 35°2θ, with a step of 0.03°2θ and a step time of 1.5 seconds.

3.3. SEM-Backscatter Electron images and Electron microprobe

Mineral petrography was carried by optical microscopy and a Merlin Compact ZEISS scanning electron microscope (SEM) equipped with backscattered electron (BSE) detector BSD4 at the Institut des Sciences de la Terre, Orléans (ISTO). The SEM-BSE was operated at 15 kV voltage and a dwell time of 50 ms. Backscattered electron images were further processed with the software ImageJ (Schneider et al., 2012) to semi-quantify the amount of each mineral phase and to prepare phase maps.

The chemical composition of the main mineral phases was determined by using a Cameca SX Five electron microprobe equipped with five wavelength-dispersive spectrometers (WDS), housed at ISTO-BRGM joint facilities in Orléans. Measurements were performed at 15 kV voltage, a 10 nA beam current and a 1 µm spot size. Analyzed elements were Si, Ti, Al, Fe, Mn, Mg, Ca, Na and K. The standards used for calibration were MgO (Mg), albite (Si, Al), andradite (Ca), orthoclase (K), $MnTiO_3$ (Mn, Ti) and hematite (Fe). For the elemental maps, the step size and dwell time were 1 µm and 150 ms, respectively. The maps were processed using the software XMapTools (Lanari et al., 2014).

3.4. Thermobarometric estimates

The crystallization temperature of chlorite was estimated with the chlorite-quartz-H_2O thermodynamic model and the parameters described in Vidal et al. (2006). Pressure was estimated via equilibrium with illite using the solid solution model from Dubacq et al. (2010). The approach relies on the phengite-chlorite-quartz model first presented by Vidal & Parra (2000) and applied to metapelites over a wide range of conditions from LP-LT (Árkai et al., 2003; Battaglia, 2004) to HP-LT terrains (e.g., Plunder et al., 2012). In chlorite and mica, substitutions are modeled with end-members. The model accounts for the following substitutions: $Fe=Mg^{2+}$; Tschermak $[Si+(Mg,Fe^{2+})=Al^{IV}+Al^{VI}]$ in illite and chlorite; di/trioctahedral $[\square^{VI}+Al^{VI}+Al^{VI}=3(Fe^{2+},Mg)]$ in illite and chlorite, and pyrophyllitic $[(Na,K)+Al=\square^{XII}+Si]$ and paragonitic $[K=Na]$ in illite (Dubacq et al., 2010; Masci et al., 2019; Vidal & Parra, 2000; Zane et al., 1998). Incorporation of water in the interlayer space of low-temperature illite is modeled via a vacancy-water $[\square=H_2O]$ substitution (see Dubacq et al., 2010). The resulting set of solid solution end-members is pyrophillite (Prl), hydrated pyrophyllite ($Prl{\cdot}1H_2O$), muscovite (Ms), Mg- and Fe-celadonite (Mg-Cel and Fe-Cel) for illite, and clinochlore (Clin), daphnite (Daph), sudoite (Sud), Fe- and Mg-amesite (Fe-Am and Mg-Am) for chlorite. Additional phases are quartz (Qtz) and H_2O with an activity set at unity. With this set of phases, 124 reactions may be written, out of which six are independent. Equilibrium is inferred when independent reactions appear reasonably close to one another in P-T space (e.g., less than 20°C and 1 kbar).

3.5. Raman spectroscopy

From each locality where deformation structures were studied, a thick section oriented in the X-Z plane of kinematic reference was prepared from metasedimentary samples for the purpose of RSCM. Analyzed particles were chosen far from shear bands to avoid shear-enhanced thermal maturation of carbonaceous material.

A Raman Renishaw InVia Reflex micro-spectrometer was used at BRGM, Orléans. A silicon standard was used for calibration. The light source was a 514.5 nm Ar laser with a power of ~1 mW, focused by a Leica DM2500 microscope at a magnification of 100x. The signal was analyzed by a CCD NIR/UV detector. 15-20 points were analyzed per sample on 150-200 µm thick, polished sections. The final deconvolution was made following the method of Lahfid et al. (2010), applicable for the temperature range from ~200°C to ~320°C. Raman spectra were processed with the software PeakFit 4.12 for subtracting the baseline and fitting each corrected spectrum with five Lorentzian bands. From the area below five Lorentzian bands, RA1 ratio was calculated by the equation RA1 = (D1 + D4) / (D1 + D2 + D3 + D4 + G). The final temperature was estimated following the equation T (°C) = 1217.6 × RA1 - 450.66 (Lahfid et al., 2010). The uncertainty of the method is ~30°C (Lahfid et al., 2010). Fifteen to twenty points were analyzed in each sample, average values and standard deviations (1σ) are reported in Table 1.

The Raman spectrum of water originates from OH stretching vibrations, which vary as a function of salinity (e.g., Caumon et al., 2014, 2015). The salinity of water-rich fluid inclusions was estimated using a Raman Renishaw InVia Qontor micro-spectrometer at CEMHTI CNRS, Orléans. A silicon standard was used for the calibration, and the light source was a 514.5 nm solid state laser. Applied power was 50 mW, focused on standards or fluid inclusions with Leica DM2700 microscope at a magnification of 100x (0.9 NA). The signal was acquired by a CCD NIR/UV "centrus" detector. Acquiring time was 60 s for each point. For calibration, 12 solutions with known NaCl molarity were prepared (0.125 M, 0.25 M, 0.375 M, 0.5 M, 0.625 M, 0.75 M, 0.875 M, 1 M, 1.25 M, 1.5 M, 1.75 M and 2 M). The solutions were placed into the borosilicate circular capillaries with outer and inner radius of 0.33 and 0.2 mm, respectively. Borosilicate capillaries are transparent to Raman signal. The Raman spectrum of the OH stretching vibrations can be divided into two sub-bands (Sun et al., 2010), strong- (HBs, with the peak centered around 3200 cm^{-1}) and weak-hydrogen band (HBw, with the peak centered around 3450 cm^{-1}). For each solution, the deconvolution process is made following the method of Sun et al. (2010) using the software PeakFit 4.12. After the baseline was subtracted, two Gaussian sub-bands were used to fit the obtained Raman Spectrum (Fig. 3a). Based on

the intensity (I) and full width at half maximum (FWHM) of each band, the equilibrium constant is calculated as:

$$K' = \frac{\left(\frac{I}{FWHM}\right)_{HBw}}{\left(\frac{I}{FWHM}\right)_{HBs}}$$

Finally, the linear correlation between K' value and salinity of prepared solutions (Fig. 3b) leads to a formula for the salinity estimation in fluid inclusions:

$$Cl^- \text{ Molarity (M)} = -0.6843*(K')^2 + 5.6135*K' - 6.3693.$$

Fluid inclusions were analyzed with the same conditions as the standards. To avoid biases due to the effect of host mineral birefringence (Caumon et al., 2015), circular polarization was applied to the beam. Additionally, the salinity of 22 fluid inclusions with wide range of salinities determined by Raman Spectroscopy were also measured by microthermometry by using a Linkam THMSG600 heating-cooling stage (Fig. 3c), wherein the salinity was estimated using the last ice-melting temperature (Bodnar, 1993).

3.6. Decrepitation of fluid inclusions

Qualitative chemical analysis of major cations and anions in individual fluid inclusions was carried out from evaporate mounds after decrepitating fluid inclusions, following the method by Kontak (2004). Double-polished quartz sections were rapidly heated by THMS-600 Linkam stage to 500-600°C and quenched for 5-15 minutes, until decrepitation was observed. The system was then rapidly cooled down to room temperature. The chemical maps of evaporate mounds were acquired by SEM-EDS at the voltage of 15 kV and a dwell time of 25 ms. In addition, the chemical composition of individual evaporate crystals was determined by using a Cameca SX Five electron microprobe, housed at ISTO-BRGM Orléans, that is equipped with five wavelength-dispersive spectrometers (WDS). The conditions used for individual crystal analyses were a 15 kV voltage, a 10 nA beam current and a 1 µm spot size. Up to 10 points were analyzed in each mound. Results were recalculated by removing SiO_2 as it is recognized as from the host quartz, and then normalizing the totals to 100%. However, acquired results are semi-quantitative due to devolatilization and loss of certain species during the decrepitation process.

4. Results

4.1. Raman Spectroscopy of carbonaceous material

Peak-metamorphic temperatures obtained by RSCM are reported in Table 1 and examples of deconvoluted spectra are provided in Fig. 4.

Temperatures for two samples from the Kodiak Landward Belt from Uyak Bay are 251 ± 9℃ (KO17A) and 240 ± 9℃ (KO17E). Samples from the Kodiak Central Belt show narrow range of temperatures from 327 to 340℃. For three samples from the Kodiak Seaward Belt determined peak-temperatures are 300 ± 19℃ (KO11), 348 ± 28℃ (KO12B), and 344 ± 16℃ (KO45C).

A sample HN65 from the Hyuga Tectonic Mélange has a recorded temperature of 228 ± 16℃, whereas samples from the Foliated Morotsuka (Samples 18NOB13, 18NOB22A, HN143, HN243, HN247, and HN285) experienced peak-temperatures of 339 ± 26℃. The results acquired as part of this study for samples from the Shimanto Belt are consistent with previously reported RSCM results (Palazzin et al., 2016; Raimbourg et al., 2017, 2018).

Peak temperatures obtained for higher-grade samples (from the Kodiak Central Belt and Foliated Morotsuka) are around or slightly above the range of the method of Lahfid et al. (2010). However, due to the presence of the D4 band and the absence of the D2 band in the Raman spectra (Fig. 4), the method of Lahfid et al. (2010) is more suitable than of Beyssac et al. (2002).

Therefore, the Kodiak Landward Belt (KLB) and the Hyuga Tectonic Mélange (HTM) are grouped as lower-grade units, whereas the Kodiak Central Belt and the Foliated Morotsuka represent higher-grade units.

4.2. Microstructures and mineral petrography

4.2.1. Lower-grade units

In Kodiak and the Shimanto Belt, lower-grade metapelites (230-260℃) show three different compositional and microstructural domains: pelitic matrix, quartz ribbons, and extensional veins (Fig. 5a). Phyllosilicates are the most abundant phases in the matrix, with clusters of fine-grained illite (illite hereby refers to minute dioctahedral aluminous phyllosilicates with composition on the muscovite-pyrophillite binary; Dubacq et al., 2010) and chlorite (Fig. 5b-c). The grain size of chlorite varies between 2.5-60 µm (Fig. 5b), and increases up to 100 µm when in contact with quartz ribbons. The grain size of illite is in the range 1-24 µm (Fig. 5b) in the matrix, whereas aggregates of illite up to 120 µm are present close to quartz ribbons. Detrital plagioclase and quartz are present in the matrix (Fig. 5b), as well as accessory phases such as framboidal pyrite, calcite, apatite and Ti-oxides. The foliation (S_1) in the pelitic matrix is defined by compositional layering (scaly fabrics; Ramirez et al., 2021; Vannucchi, 2019), enriched in fine-grained phyllosilicates, sulfides, Ti- and Fe-oxides (Fig. 5a, 5d). Occasionally, thin shear bands composed principally

of elongated individual crystals of chlorite (Fig. 5c) and to a lesser extent illite and/or quartz grains, cut the main foliation at low angles. These shear bands form an anastomosing network and indicate non-coaxial shearing (Fig. 5a).

Extensional veins, commonly oriented perpendicular to the foliation, are made of blocky quartz and to a lesser extent calcite (Fig. 6a). Quartz crystals in lower-grade veins occasionally display growth rims, with crystal facets oriented towards the center of the vein. Occasionally quartz crystals are elongated parallel to the foliation (Fig. 6b). Bulging, as a mechanism of dynamic recrystallization, is observed sparsely. Calcite display characteristic undeformed twinning (Fig. 6a; Type I according to Ferrill et al., 2004). Ribbons containing quartz ± calcite ± small flakes of chlorite are elongated parallel to the main foliation (Fig. 5a). Calcite, when present, occurs as late fill of the vein and is mildly altered.

4.2.2. Higher-grade units

In higher-grade samples of the KCB and FM (Table 1; 330-350°C), the main mineral phases forming the matrix are illite, chlorite, quartz and plagioclase. The foliation (S_1) is penetrative and underlined by phyllosilicates (Fig. 5g-h), and it is locally disturbed by 5-20 µm thick shear bands containing illite, chlorite, Ti-oxides, and sulfides. Whenever present, plagioclase and quartz crystals are flattened and elongated parallel to the foliation (Fig. 5h). A secondary crenulation cleavage (S_2) is present only in the vicinity of shear bands. The average grain size in the pelitic matrix of higher-grade samples is larger than in lower-grade samples. In the KCB for instance, chlorite crystals are generally in the range of 5 to 400 µm and up to 775 µm in length when in contact with shear bands, whereas illite crystals reach 1-80 µm in the matrix and up to 320 µm closer to shear bands (Fig. 5e-f). In the FM, matrix illite and chlorite have significantly larger grain size than in the KCB, ranging between 30-500 µm and 50-700 µm, respectively (Fig. 5f). Accessory phases in the matrix are apatite, pyrite, calcite, anatase and titanite. Sulfides are locally oxidized into goethite, with preserved pyrite crystal shapes. Scaly fabrics are enriched in micrometric anatase, apatite and Fe-oxides (Fig. 5i-j), and occasionally act as shear planes displacing the main foliation and quartz ribbons.

In higher-grade units, quartz ribbons are boudinaged and occasionally folded. The neck of boudins is composed of illite, chlorite and elongated quartz crystals. Shear veins and Mode 1 quartz veins cutting across the foliation are dominantly made of quartz and display crack-seal microstructure (Fig. 6c). Bulging is recognized as a dominant mechanism of dynamic recrystallization in quartz from higher-grade veins. Subgrain rotation is observed and is more prominent in the FM than in the KCB. In addition to quartz,

veins contain calcite, chlorite, and albite (Fig. 6e-f). Deformed calcite is characterized by curved and lensoid twins (Fig. 6d; Type III according to Ferrill et al., 2004). In a few of the studied veins, clusters of vermicular chlorites are sparsely distributed, as well as euhedral albite crystals (Fig. 6f).

Locally, mineralogical variations are observed in correspondence with the microstructures. In the matrix in the contact with some shear bands, quartz and plagioclase grains are almost completely absent (Fig. 5e-f). Fig. 6f shows the host rock with few micrometric albite crystals, whereas larger crystals (up to 0.2 mm) are found in the shear band. Similar features were observed in the veins from the KCB, with veinlets apparently located on one side of the main vein (Fig. 7a). On the side with veinlets, the crenulation cleavage (S_2) is found close to the contact (Fig. 7c), and disappears further from the shear band (Fig. 7d). The amount of quartz decreases towards the vein, and quartz is absent from the zone with crenulation cleavage (Fig. 7e). Anatase also appears to be formed synchronously with crenulation cleavage (Fig. 7g), as it is concentrated in crenulation cleavage planes with apatite. However, in zones where only the main foliation present titanite is found (Fig. 7h).

4.3. Whole-rock chemistry

Whole-rock major element compositions are presented in Table 2. In samples from the Kodiak complex, oxide concentrations and LOIs are in the following ranges: SiO_2 - 54.76% to 69.90%; TiO_2 - 0.60% to 1.00%; Al_2O_3 - 12.22% to 20.27%; Fe_2O_3 - 6.87% to 8.82%; MgO - 1.94% to 3.29%; CaO - 0.33% to 1.28%; Na_2O - 0.97% to 2.77%; K_2O - 1.48% to 3.61%; SO_3 - 0.02% to 0.37%; and LOI - 3.16% to 5.23%. Major elements and LOI in samples from the Shimanto Belt are in the range of: SiO_2 - 61.72% to 75.83%; TiO_2 - 0.34% to 0.70%; Al_2O_3 - 10.30% to 18.15%; Fe_2O_3 - 5.41% to 7.34%; MgO - 1.49% to 2.44%; CaO - 0.06% to 0.88%; Na_2O - 1.11% to 3.33%; K_2O - 1.44% to 3.29%; SO_3 - 0.01% to 1.89%; and LOI - 2.61% to 5.08%.

No clear trend is apparent in major element compositions as a function of temperature, except for weak positive correlation for K_2O, MgO and Fe_2O_3, and strong negative correlation for SO_3. The normalization of oxides to TiO_2 (assumed as an immobile oxide) as a function of temperature of metamorphism, reveals no clear trends as well (Fig. 8).

4.4. X-Ray diffraction and phase quantification

X-Ray diffraction on bulk rocks confirmed the major phases observed using optical and electronic microscopy (Table 3; Fig. S1): illite, quartz, plagioclase and chlorite, and provide evidence of smectite-illite

mixed layers in lower-grade samples and in the higher-grade sample 18NOB23B. Accessory phases are calcite and pyrite, and serpentine in three lower-grade samples and in one higher-grade sample (Sample HN243). Magnesite, siderite and kaolinite are detected in individual samples (Table 3).

Quantitative phase proportions based on the method of Rietveld (1969) reveal that the main rock-forming mineral phases of lower temperature samples (230-260°C) are illite/mica (23-48%), quartz (17-43%), plagioclase (10-20%), chlorite (0-14%) and smectite-illite mixed layers (0-8%). Minor phases include serpentine (detected in three samples, 1.6-3.4%) and kaolinite (only in one sample - HN64, 4%). Higher temperature samples (~330-350°C) show similar proportions of main phases: illite/mica (21-42%), quartz (16-34%), plagioclase (5-25%) and chlorite (15-24%). The amount of smectite-illite mixed layers in the sample 18NOB23B is estimated as 1.5% and 1.8% of serpentine is estimated in the sample HN243.

4.5. Mineral composition

Representative analyses of illite and chlorite, as well as calculated structural formulas are listed in Table S1, whereas all acquired analyses are listed in Table S2 of the Supplementary information. In all lower- and higher-grade samples plagioclase is albitic (X_{Ab}>0.98), with only traces of K and Ca. In contrast, K-bearing phyllosilicates and chlorites show compositional variations correlated with peak-metamorphic temperatures.

4.5.1. K-bearing phyllosilicates

More than 20 grains of mica were analyzed in the matrix of each sample. Calculation of structural formulae on the basis of 11 oxygen atoms shows that analyses correspond to dioctahedral mica, which is in agreement with XRD data. The sum of the interlayer cation is variable, ranging between 0.45 and 0.95 in lower-grade samples, and between 0.77 and 0.95 in higher-grade samples (Fig. 9a). Values lower than 1.0 indicate that illite-smectite mixed layers are probably present.

In lower-grade samples (from KLB and HTM units), K is the dominant alkali (KLB: 0.43-0.81 apfu; HTM: 0.43-0.88 apfu), with secondary Na (KLB: 0.02-0.38 apfu; HTM: 0.01-0.32 apfu; Fig. 9a). Micas contain 0.27 vacancies pfu in average for KLB (0.09-0.44 pfu) and 0.26 pfu for HTM (0.05-0.55 pfu). Higher-grade samples (from KCB and FM units) show homogenous compositions among samples (Fig. 9e). The proportion of K increases in comparison with lower-grade samples (KCB: 0.74-0.89 apfu; FM: 0.74-0.96 apfu), whereas the amount of Na decreases (KCB: 0.01-0.04 apfu; FM: 0.01-0.06 apfu). Remaining interlayer vacancies are estimated to be around 0.09-0.22 pfu for the KCB and 0.1-0.24 pfu in the case of FM (Fig. 9a).

Octahedral sites are dominantly occupied by Al, without correlation to temperature (lower-grade: KLB av. 1.79 apfu, range 1.55-1.92; HTM av. 1.82 apfu, range 1.62-1.92; higher-grade: KCB av. 1.77 apfu, range 1.64-1.82; FM av. 1.73 apfu, range 1.54-1.81). Remaining octahedral position is occupied by Fe and Mg. In KLB, Fe is more abundant than Mg (av. FeO 2.25 wt.% and av. MgO 1.6 wt.%), whereas in HTM the proportion of Fe and Mg are similar (av. FeO 1.4 wt.% and av. MgO 1.45 wt.%). There is similar amount of Fe and Mg in higher-grade samples (KCB: av. FeO 1.71 wt.% and av. MgO 1.73 wt.%; FM: av. FeO 2.2 wt.% and av. MgO 1.9 wt.%).

In the tetrahedral site, there is no systematic changes in the Al-Si substitution with increasing temperature. The average SiO_2 content in lower-grade samples is 49.62 wt.% (3.13-3.65 apfu) and 49.74 wt.% (3.11-3.67 apfu) for KLB and HTM, respectively, whereas SiO_2 in higher-grade samples shows narrower concentration variations - 49.32 wt.% in average (3.24-3.37 apfu) for the KCB and 47.57 wt.% in average (3.10-3.37 apfu) for the FM.

4.5.2. Chlorite

The structural formulae of chlorite are calculated on the basis of 14 oxygen atoms. Chlorite in lower-grade samples exhibits chemical variations (Table S1 in the Supplementary information), with the magnesium number (X_{Mg}) generally in the range of 0.3-0.45 (Fig. 9d). Higher-grade chlorite has similar X_{Mg} compared to lower-grade chlorite but appears more homogenous. Lower-grade chlorite contain a greater number of vacancies (0.23 ± 0.08 and 0.21 ± 0.06 pfu in KLB and HTM, respectively) than in higher-grade chlorite (0.09 ± 0.06 pfu and 0.08 ± 0.06 pfu for KCB and FM, respectively; Fig. 9c). Tetrahedral Al increases with temperature from 0.60-1.27 to 1.02-1.39.

All analyzed grains in higher-grade samples show high clinochlore (X_{clin} 0.24 ± 0.01 and 0.21 ± 0.03 for the KCB and the FM, respectively), daphnite (X_{daph} 0.35 ± 0.01 and 0.34 ± 0.01 for the KCB and the FM, respectively), and amesite (X_{am} 0.34 ± 0.06 and 0.38 ± 0.11 for the KCB and the FM, respectively) proportions, with a low sudoite proportion (X_{sud} 0.07 ± 0.06 and 0.03 ± 0.03 for the KCB and the FM, respectively; Fig. 9f).

4.5.3. Multi-phase equilibrium model for the higher-grade units

In lower-grade samples, the multi-phase equilibrium model did not permit the identification of equilibrium pairs, and hence pressure-temperature conditions could not be estimated. In higher-grade samples, equilibrated pairs of illite and chlorite have been identified (Fig. 10a). Fig. 10c shows the pressure-temperature conditions for equilibrium of illite-chlorite pairs sampled from Fig. 9e-f. The results

from samples from the KCB spread over the range 250-350°C and 2-4 kbar, with a global average of 327 ± 21°C and 3.0 ± 0.4 kbar. In the FM, the results spread over the range 300-350°C and 3-4.5 kbar, with average values of 320 ± 14°C and 3.9 ± 0.4 kbar (Fig. 10c).

4.6. Fluid inclusions

4.6.1. Petrography of fluid inclusions

Quartz in the veins is characterized by high abundance of fluid inclusions (Fig. 11a-b). Veins from lower-grade units contain two types of primary fluid inclusions (Fig. 11c) interpreted to be the result of fluid immiscibility (Raimbourg, 2015; Vrolijk et al., 1988): (1) One-phase CH_4-rich fluid inclusions with a size of up to 20 µm and negative crystal shapes. These CH_4-rich fluid inclusions are randomly oriented in the host quartz. (2) Smaller (<10 µm) two-phase H_2O-rich fluid inclusions with various shapes including round, squared to irregular (Fig. 11c). The small vapor bubble is dominated by CH_4 (Raimbourg et al., 2018). In zones characterized by stretched quartz, fluid inclusions (both CH_4-rich and H_2O-rich) appearing as pseudo-secondary and are commonly in fracture healing planes perpendicular to the orientation of the elongation direction of quartz (Fig. 6b; Palazzin et al., 2016; Raimbourg et al., 2018).

In the higher-grade quartz veins, only one set of primary fluid inclusions is observed. The primary fluid inclusions contain two phases and are H_2O-rich with a V/L ratio of 0.1-0.15 (Fig. 11d). A size of inclusions rarely exceeds 10 µm. The vapor bubble contains minor amount of CO_2 and CH_4 (Raimbourg et al., 2018). Secondary fluid inclusions are common, aligned as healed fractures or trails of tiny one-phase fluid inclusions without systematic orientation of trails.

4.6.2. Fluid inclusion salinity

The salinity of the fluid inclusions has been estimated in primary two-phase fluid inclusions and in a few secondary fluid inclusions (Fig. 12). In veins formed at lower temperatures, the salinity of primary fluid inclusions is often lower than ~3.5 wt.% NaCl eq., which is the salinity of seawater (Fig. 12). In KLB for instance, primary fluid inclusions in samples: KO17A and KO17H yield average salinities of 2.1 ± 0.9 wt.% NaCl eq. and 2.1 ± 1.1 wt.% NaCl, respectively. Similarly, primary fluid inclusions in samples NOB_11C and NOB_8B of the HTM yield average salinities of 2.2 ± 0.9 wt.% NaCl eq. and 1.2 ± 0.6 wt.% NaCl eq., respectively. A small proportion (<10%) of measured primary fluid inclusions show higher salinity than seawater. On the other hand, in higher-grade veins the average salinity of primary fluid inclusions is more variable and higher than in those of lower-grade veins, often exceeding the salinity of seawater (Fig. 12). This is the case in the KCB, for which primary fluid inclusions in samples KO32F, KO32A, KO32B, and

KO33A2 yield average salinities of 5.2 ± 2.5 wt.% NaCl eq., 2.9 ± 0.9 wt.% NaCl eq., 3.9 ± 1.8 wt.% NaCl eq., and 3.5 ± 1.4 wt.% NaCl eq., respectively. In the FM, samples NOB_23B, NOB_13F and NOB_4C yield average salinities of 3.7 ± 1.4 wt.% NaCl eq., 3.4 ± 1.3 wt.% NaCl eq., 3.3 ± 0.7 wt.% NaCl eq., respectively. The salinity of secondary fluid inclusions from both localities is below 1 wt.% NaCl eq., in average 0.5 ± 0.3 wt.% NaCl eq. (Fig. 12).

4.6.3. Fluid inclusion chemistry

SEM-EDS analyses of fluid inclusions in evaporite mounds (Fig. S2) in lower-grade veins show the presence of Na, K, Ca, Mg and Fe as cations, and Cl and S as anions (Table S3; Fig. 13a). EPMA point analysis revealed that the Ca/Na ratio is dominantly >1 (Fig. 13b), except for the sample NOB_13F and one evaporate mound in the sample NOB_23B where NaCl is the dominant compound (Fig. 13a). The amount of Fe and Mg varies between each analyzed mound (Fig. 13a), ranging from ~1.5 to ~47% and from ~1.5 to ~42%, respectively. As shown in Fig. 13, S and Cl are dominant anions, and the largest group of evaporate mounds (~75%) are characterized by SO_2/Cl ratio equal or higher than 1 (Fig. 13c).

5. Discussion

5.1. Changes in mineralogy as a function of temperature

Our analyses from Kodiak and Shimanto reveal that metapelites of two studied accretionary prisms underwent a similar evolution of mineral proportions with peak-metamorphic temperature. In both cases, the most prominent mineral change is an increasing proportion of chlorite relative to other phyllosilicates with increasing temperature (Table 3; Fig. 14a). Ramirez et al. (2021) also reported an increase in the chlorite/phyllosilicates ratio with increasing temperature in metapelites of the Mugi and Makimine mélanges from the Shimanto Belt, which experienced peak-metamorphic temperatures of ~150-350°C. Additionally, Kameda et al. (2011a) described an increasing chlorite content from undeformed to deformed metasediments of the Kitagawa Group in the Shimanto Belt, which evolved in tandem with more pervasive foliation. Because both the undeformed and deformed part of the Kitagawa Group experienced the same metamorphic temperatures (Kameda et al., 2011a), the crystallization of chlorite must be facilitated not only by a temperature increase, but also by deformation. The same conclusion was reached by Casciello et al. (2011) and Famin et al. (2021) for the transformation of smectite into illite, which is enhanced in deformation microstructures within metapelites even at isothermal conditions.

The last important mineral reaction observed is the oxidation of pyrite. Pyrite is present in both lower- and higher-grade samples. In addition, in higher-grade samples pyrite is partly or completely oxidized to goethite. The main question is whether sulfide oxidation occurred during metamorphism or due to the samples being exposed at the surface. Goethite is reported to be hydrothermal phase (e.g., Makvandi et al., 2021), which is further supported by experimentally derived work wherein goethite is stable under low to moderate pressures compatible with the metamorphic conditions of the present work (Majzlan et al., 2003). The oxidation of pyrite at peak conditions is also further supported by the precipitation of Fe-oxides within the scaly fabrics that formed during metamorphism (Fig. 5i-j; see also Ramirez et al., 2021). Finally, sulfide oxidation is matched by a significant drop of SO_3 on whole-rock scale with increasing temperature (Fig. 8). The remobilization of iron at depth by dissolution of pyrite within the fluid is also attested by our analysis of the composition of the metamorphic fluid. In decrepitated mounds from the higher-grade veins, S is detected qualitatively by the SEM-EDS maps as well as in EPMA point analysis, and in many analyzed mounds it is predominant over chlorine (Fig. 13).

The progressive breakdown of pyrite in metasedimentary units is described as a result of a change in the redox state of the rocks (Dubessy et al., 1983; Ferry, 1981; Frey et al., 1980; Hall, 1986). Similar observations to those of the present study are reported in the external part of the Central Alps, where upon temperature increase, the gas dissolved within the metamorphic fluid changed from CH_4 to CO_2 and H_2O, in connection to reduction reactions in the Fe-bearing phases, biotite and pyrite (Tarantola et al., 2007, 2009). Such a transition in the nature of the gas is proposed to occur at temperatures ~270°C (Tarantola et al., 2009), and we observed it as well in fluid inclusions from both Kodiak and Shimanto (Raimbourg et al., 2018; Fig. 11).

As previously discussed, the main mineralogical change in the metapelites that occurred with an increase in temperature is an increase in chlorite relative to other phyllosilicates (Fig. 14a). Chlorite is the dominant Fe-Mg phase in the metapelites and an important question is whether the local Fe and Mg source is sufficient to support the transformation of phyllosilicates into chlorite, or if an external supply of Fe and Mg is needed. It is reported that diagenetic chlorite can form as a coproduct of the smectite-to-illite transformation during burial at temperatures as low as 70°C (Ahn & Peacor, 1985; Drief & Nieto, 2000; Hower et al., 1976; Muffler & White, 1969), or by the breakdown of smectite and kaolinite to form chlorite and illite (Boles & Franks, 1979). In both of the reactions described above, illite is the predominant product along with ~30% chlorite (Boles & Franks, 1979; Hower et al., 1976). These reactions can explain the formation of chlorite in lower-grade samples from this study (below 260°C), wherein the chlorite content

is 19-27% of all phyllosilicates (Table 3) and illite-chlorite intergrowth is observed (Fig. 5b). Also, among the minor phases detected by XRD are smectite-illite mixed layers, serpentine and kaolinite in lower-grade samples (Table 3), which are proposed to be the precursor for chlorite (Boles & Franks, 1979). Kameda et al. (2011a) proposed that chlorite crystallized from Fe-bearing berthierine, a category of inherited serpentine minerals that are metastable under low-metamorphic conditions. In this study, we have detected serpentine by XRD in lower-grade samples (Table 3). We propose that the chlorite in samples corresponding to temperatures of 230-260℃ is inherited from earlier smectite-to-illite transformation as well as a product of destabilization of serpentine.

As smectite-illite mixed layers transform into illite-muscovite during prograde metamorphism with increasing temperatures, the occupancy of interlayer site increases with as pressure and temperature increase and hence additional potassium is required (Fig. 9a). Taking the illite composition from Table S1 (Samples KO17A and KO33 as representatives), the following reaction is observed:

$$1.03\ K_{0.61}Na_{0.15}Al_{1.72}Mg_{0.18}Fe_{0.17}Si_{3.35}Al_{0.65}O_{10}(OH)_2 + 0.23\ K^+ =$$

$$K_{0.86}Na_{0.02}Al_{1.74}Mg_{0.15}Fe_{0.1}Si_{3.31}Al_{0.69}O_{10}(OH)_2 + 0.07\ Fe^{2+} + 0.12\ SiO_2 + 0.13\ Na + 0.03\ Mg + 0.02\ H_2O + 0.28\ O_2 \qquad \text{(Eq. 1)}$$

A small fraction of iron, magnesium and water is released during the smectite-to-illite transformation. However, this reaction alone cannot explain the increase in the amount of chlorite at higher temperatures, nor the textural observations, such as chlorite rims around pelitic matrix or an enrichment in the crenulation cleavage zones (Fig. 5e, 6e). Several studies report the chloritization of micas during interaction with hydrothermal fluids (e.g., De Parseval et al., 1994; Komninou & Sverjensky, 1995; Tarantola et al., 2007, 2009), where muscovite or biotite react with Fe^{2+}, Mg^{2+} and H_2O, creating chlorite and releasing significant amount of K^+ and H^+. During this study, we observed chlorite only as bimineralic chlorite-illite rims at the contact of the veins with the matrix (Fig. 5e, 6f). These rims are consistent with fluids acting as catalyzers of chlorite crystallization. As there is no systematic Mg and/or Fe increase in the host rock with temperature, the source of both elements is likely local. From the chemical composition of illite and chlorite from the zone with chlorite rims presented in Fig. 6f (Sample KO33), the crystallization of chlorite appears to proceed through the following reaction:

$$1.18\ K_{0.88}Na_{0.02}Al_{1.74}Mg_{0.19}Fe_{0.1}Si_{3.31}Al_{0.68}O_{10}(OH)_2 + 2.5\ Fe^{2+} + 1.6\ Mg^{2+} + 6.23\ H_2O =$$

$$Fe_{2.63}Mg_{1.82}Al_{1.43}Si_{2.71}Al_{1.43}O_{10}(OH)_8 + 1.04\ K^+ + 0.02\ Na^+ + 1.2\ SiO_2 + 6.82\ H^+ \qquad \text{(Eq. 2)}$$

where illite reacts with water, Fe and Mg creating chlorite and releasing Si, K and Na into the fluid. Because more K is required in illite in higher-grade samples (Fig. 9a), the amount of K released during this reaction is likely incorporated into remaining or newly formed illite (Eq. 1).

5.2. Mass transfers

Even though several mineral reactions were recognized, whole-rock chemistry (Fig. 8) revealed no significant chemical variations in the pelitic matrix as a function of peak-metamorphic temperatures (except for a large decrease in SO_3), therefore elements were redistributed between metamorphic minerals. However, specific zones of the matrix, such as in the vicinity of the veins, are characterized by changes in mineralogy that imply mass transfer at a small scale. In such zones, as presented in Fig. 6 and 7, the matrix in contact with veins is characterized by the absence of quartz and a lower proportion of albite than in unaffected zones. Mass-balance calculations for specific zones of the higher-grade samples (zones with crenulation cleavage in the contact with veins and further from veins; Table S4), presented after normalization to TiO_2 (e.g., Fig. 8), show a decrease in SiO_2 and Na_2O counterbalanced by an increase in FeO, MgO, K_2O and LOI. Hence, SiO_2 loss is the result of the removal of SiO_2 from the matrix and preservation of other mentioned elements. This can be interpreted as a result of dissolution of quartz and albite and the crystallization of chlorite and illite (e.g., Fig. 7; Fisher et al., 1995; Fisher & Brantley, 1992). Other zones in the pelitic matrix where mass transfer occurred are the scaly fabrics (Fig. 5d, 5i), as they are enriched in Fe- and Ti-oxides with fine-grained illite and chlorite and depleted in quartz and albite. Similar observations were made in metapelites from the Shimanto Belt (Kawabata et al., 2007; Ramirez et al., 2021), where the progressive formation of scaly fabrics (their abundance and depletion in mobile elements) is described as being facilitated by the temperature increase in addition to deformation. For the elements depleted in scaly fabrics, such as SiO_2 or Na_2O, Ramirez et al. (2021) proposed that the mass transfer occurred along the planes of the scaly fabrics to the veins, where quartz and albite precipitated. A similar process is observed in the present work, wherein the mass transfer occurs from the host rock in the immediate vicinity of the vein towards the vein itself, which is interpreted as a site of dilation and preferential precipitation by Brantley & Fisher (1997).

Additionally, because the two proposed reactions (Eq. 1 and Eq. 2) release SiO_2, one can wonder whether this source of silica is a major contribution to produce the quartz veins observed in the field (Fig. 2). For 100 g of the matrix, if 10% of the illite transformed into chlorite (with the chemical composition from Table S1) approximately 3 g of SiO_2 will be released. Comparing this value with the dissolution of quartz and albite observed in the matrix contacting the veins, such as in Fig. 5e and Fig. 7, the complete

565 dissolution of quartz and albite (both constituting between 10 and 20% of the rock) releases about 17 to
566 34 g of SiO_2. Therefore, most of the silica precipitated in the veins stems from the dissolved quartz and
567 albite in the host rock, whereas the production of SiO_2 by metamorphic reactions is only a secondary
568 factor. Taken together, both sources can produce 20 to 37 g of free SiO_2 in 100 g of the matrix. Thus, the
569 mass of reactive matrix is estimated as three to five times the one of crystallized veins.

570 Given the spacing between adjacent veins, it appears that local redistribution of silica is in most instances
571 sufficient to precipitate the quartz veins observed in the field without any requirement for an external
572 source of silica. The zones with noticeably different mineralogy are limited to a thickness of <2 cm from
573 the contact with the veins. Even though the length of diffuse mass transfer is difficult to trace, mass
574 balance calculations as well as textural observations, in the examined samples are consistent with mass
575 transfer being limited to a mm- to cm-scale. Unlike in examples of similar lithologies where an external
576 fluid is required, such as the Otago Schist (Breeding & Ague, 2002) or the Catalina Schist (Bebout, 1991,
577 1993; Penniston-Dorland et al., 2012), this work supports the idea of locally derived material forming the
578 veins in the Kodiak complex and the Shimanto Belt (Brantley & Fisher, 1997; Fisher et al., 1995; Ramirez
579 et al., 2021).

580

581 **5.3. P-T conditions of metamorphism**

582 Due to difficulties such as small grain size or the lack of equilibrium between newly formed phases,
583 estimating pressure-temperature conditions in low-grade metamorphic rocks is often challenging. Despite
584 these challenges, our study succeeded in estimating peak-metamorphic temperatures in the metapelites
585 from two independent techniques, RSCM and chlorite thermometry. Both techniques yield similar results
586 and confirm that chlorite formed at peak-temperatures (Fig. 10c). The illite-chlorite multi-phase
587 equilibrium model indicates that both phases are metamorphic and not inherited. Additionally, textural
588 observations are consistent with the precipitation of albite in veins at peak-metamorphic conditions,
589 because it has been observed within chlorite rims (Fig. 6f). Furthermore, newly formed chlorite and albite
590 are found at the contact with and in the crack-seal veins, which indicates that the precipitation of chlorite
591 and albite occurred contemporaneously with deformation. This confirms that the quartz in crack-seal
592 veins also crystallized at peak conditions, as inferred from structural analysis of the veins (Fisher &
593 Brantley, 2014; Raimbourg et al., 2021). Consequently, the crack-seal structures described in these veins
594 (Raimbourg et al., 2021; Ramirez et al., 2021) were also formed at temperatures ~300-350°C.

The RSCM temperature results in the KLB are ~250°C, which is upper limit for homogenization temperatures (215-255°C) derived from fluid inclusions (Vrolijk et al., 1988). For the KCB, our estimate of 2.5-3.5 kbar, 300-340°C is slightly higher than the average temperature of 280°C obtained by Brantley & Fisher (1997) using $\delta^{18}O$ thermometry on quartz, mica, and chlorite (Brantley & Fisher, 1997). A possible explanation to this discrepancy is that $\delta^{18}O$ thermometry is more sensitive to low-temperature re-equilibration, due to intermineral oxygen diffusion (e.g., Sharp & Kirschner, 1994), than RSCM and chlorite thermometry. In the case of the Shimanto Belt, our P-T estimate of 3.5-4.5 kbar and 300-350°C for the FM (Fig. 10c) is consistent with Toriumi & Teruya (1988) who proposed peak-metamorphic conditions at 3-5 kbar and 300-350°C based on mineral assemblages in metamafic rocks from the same unit.

Pressure and temperature results for the KCB estimated during this study point to a geotherm that is close to 30°C/km, which is in agreement with the previously proposed arguments for a warm geotherm in the subduction zone during the Cretaceous-Paleogene (Fisher & Byrne, 1992; Sample & Moore, 1987; Vrolijk et al., 1988). This geotherm is attributed to a ridge subduction less than 12 million years after the accretion of thick turbiditic sequences. Based on coexisting H_2O- and CH_4-rich fluid inclusions in extensional veins, Vrolijk et al. (1988) estimated a geothermal gradient of ~20-25°C/km in the Uyak Complex, Kodiak and Ghost Rocks Formations, and concluded that these units were buried to a depth of 10-14 km. Our geotherm estimate suggests that the KCB has been buried to a depth of 10-12 km. Furthermore, if the geothermal gradient remained constant during accretion, all of the units from the Kodiak complex in this study were buried to a depth of 7-12 km, depending on the peak-metamorphic temperature.

5.4. Effect of mineral reactions on fluid composition and the fluid budget

Initially during sediment burial, compaction and cementation reduce the porosity from several tens of vol.% to a few vol.% (e.g., Saffer & Tobin, 2011). Simultaneously, the pore fluid (originally seawater) becomes diluted by reactions such as smectite-to-illite transformations, which release fresh water (e.g., Colten-Bradley, 1987; Kastner, 1981; Kastner et al., 2014; Moore & Vrolijk, 1992; Perry & Hower, 1970; Spinelli, 2004). These transformations mostly occur in the temperature range 50-150°C, but may extend up to 250°C (Kameda et al., 2011b; Kastner et al., 2014). In several examples of metasedimentary rocks from paleo-accretionary complexes experiencing temperatures of ~250°C, fluid inclusion salinities in syn-subduction veins are lower than seawater (Herviou et al., 2021; Raimbourg et al., 2018; Fig. 12, 14b),

which confirms this progressive dilution of the pore fluid during burial. Raimbourg et al. (2018) point to a difference in both salinities of fluid inclusions of rocks subducted to shallower and deeper than brittle-plastic transition. With increasing burial, another major change in the fluid composition occurs at the brittle-plastic transition at a temperature of ~300-350°C (e.g., Mullis et al., 1994; Raimbourg et al., 2018; Tarantola et al., 2007, 2009). At depth below this rheological limit, pore fluid salinities, as inferred from fluid inclusions in various subduction zones worldwide, become highly variable and are often higher than seawater (Herviou et al., 2021; Raimbourg et al., 2018 and references therein). This increase and scattering of salinities shallower than the brittle-plastic transition, from ~250°C to 300-350°C, is not explained to date. To interpret the increase in salinity, two possibilities can be considered: (1) Infiltration of external fluids with a high salinity; (2) Hydration reactions and uptake of low-Cl^- water in the minerals. The increase of salinity as a result of brine infiltration has been proposed for metasedimentary units in the Western Alps and explained as the infiltration of fluid from blocks of margin units containing evaporites (Herviou et al., 2021). However, in the case of the Kodiak complex and the Shimanto Belt, no evaporites have been reported and the majority of units are made of deep-trench sediments (Byrne, 1982; Fisher & Byrne, 1987; Nishi, 1988; Sakai et al., 1984; Sample & Moore, 1987). Our fluid inclusion analyses show that the salinity increase and scattering also occurs in the metapelites of Kodiak and Shimanto (Fig. 12). Thus, our mineralogical and chemical results allow us to propose an explanation for these salinity variations. Indeed, for the pelitic rocks of the two accretionary prisms, burial between 230-260°C and 330-350°C was accompanied by an increase in chlorite proportion as previously discussed.

An important issue related to chlorite crystallization is that chlorite hosts more water than smectite-illite; ~13 wt.% compared to ~6-7 wt.%, respectively (Table S2). Analyzed illite in lower-grade rocks contains about 7 wt.% of water. During formation of about 10% of chlorite, it is assumed that water from illite is incorporated into chlorite; however, there is still a need for additional water. In 100 g of a rock with composition the same as that of sample KO38 (Table S1), 10% of newly formed chlorite contains ~1.3 wt.% H_2O. Potentially inherited water from 10% of illite is ~0.7 wt.% H_2O, hence there is a deficit of 0.6 wt.%, or 1.62 vol.% H_2O. Therefore, some of the pore fluid has to provide H_2O for chlorite crystallization and as a result the salinity of pore fluid increases (Fig. 12, 14b). The amount of pore water incorporated into chlorite is highly dependent upon the initial porosity and amount of illite in the metapelite protolith, which explains the scattering of salinity increases toward high-T samples. This amount of water incorporation by illite-to-chlorite transformation is also smaller than the variability of the initial water content of metapelite, which likely, along with the amount of the carbonates in the rock, masks any correlation between LOI and temperature (Fig. 8).

The oxidation of pyrite into goethite requires water as well. As an order of magnitude estimate, the amount of initial pyrite is estimated to be roughly as 0.5-1% (Table 3). Since goethite contains ~10 wt.% of crystal-bound H_2O, the transformation of 0.5-1% of pyrite into goethite requires 0.05-0.1 wt.% H_2O, or 0.14-0.27 vol.%. Due to low abundance of pyrite, this reaction does not significantly affect the water budget. Combining the two described hydration reactions, the quantity of required fluid and the observed increase in salinity (~40%), the initial pore space is estimated at 4.4-4.7 vol.% and decreases down to 2.6-2.8 vol.%.

Beside the influence of hydration/dehydration reactions (i.e., uptake/release of H_2O from/into the pore fluid), the salinity might also reflect the uptake/release of solutes out of/into the pore fluid. During this study, qualitative analysis of evaporite mounds of fluid inclusions revealed the large variability in the chemical composition of the pore fluid (Fig. 13). In evaporate mounds, instead of Na predominance (except for one analyzed evaporate mound; 23_B mound1 in Fig. 13a), Ca is the predominant cation with various amount of Na, K, Mg and Fe (Fig. 13). Additionally, S is present in equal amount to Cl or is the predominant anion (Fig. 13). This enrichment is the consequence of pyrite oxidation. This is also supported by iron oxides localization in shear planes and a significant decrease in S in whole-rock compositions. In a similar manner, an increase of S content in the fluid inclusions along the prograde path has been described in metasedimentary rocks from the Central Alps (Rauchenstein-Martinek et al., 2016), as a result of prograde devolatilization reactions.

Another implication of our findings is that the composition of pore fluids in subducted sediments is not exclusively controlled by the release or uptake of water in minerals. The chemical evolution of fluids in sediments undergoing subduction is often simplified as a suite of salinity changes occurring in response to the release or uptake of pure water by mineral reactions, assuming NaCl as the dominant species in solution (Herviou et al. (2021) and references therein). Our study shows that other reactions, such as the oxidation of pyrite, may profoundly change the composition of pore fluids, and that S may become the dominant species in solution. Because S is a highly reactive species under certain redox conditions, this drastic evolution in the chemistry of pore fluids may generate other reactions, for instance with carbonates. Further work is required to investigate and quantify these reactions and their effect on the composition of subducted fluids.

A final implication of our study is that the transformation of illite into chlorite and the oxidation of pyrite are two reactions that transform pore water into structural water. By consuming pore fluids, these hydration reactions contribute to decrease the porosity of metapelites undergoing subduction. Because

these reactions occur in the 250-350°C temperature range, they also strongly contribute to trapping water in minerals, and thus to restrict fluid circulation in the realm of the brittle-plastic transition. As opposed to large-scale circulation and infiltration of external fluids described in several exhumed blueschist and eclogite facies complexes (Angiboust et al., 2011, 2014; Herviou & Bonnet, 2023; Muñoz-Montecinos, Angiboust, & Garcia-Casco, 2021; Spandler & Pirard, 2013; Taetz et al., 2016), results from this study support a model wherein the brittle-plastic transition is the limit between a domain of large-scale circulation of external fluids below it, and a domain of small-scale transfers of local fluids above it (Fagereng et al., 2018; Hyndman & Wang, 1993; Oleskevich et al., 1999; Raimbourg et al., 2018).

6. Conclusions

The present results show well-identified mineral equilibrium in higher-grade samples (at temperatures >300°C), whereas at lower-grade equilibrium is not achieved (at temperatures <300°C). Chlorite thermometry revealed similar temperature of crystallization as RSCM, consistent with the occurrence of mineral reactions at peak-metamorphic conditions.

Our study shows that during prograde metamorphism of subducted metapelites, in the range of 230-260°C to 330-350°C, the major mineralogical change is an increase in chlorite/illite ratio as a result of illite-to-chlorite transformation. Other reactions include the oxidation of pyrite into goethite and dissolution of titanite and precipitation of anatase.

The bulk composition of the rock is not significantly modified at a temperature range from 230-260°C to 330-350°C, which suggests limited mass transfer. Local mass transport is nevertheless observed in the vicinity of veins that formed at peak conditions. There, the matrix is depleted in quartz and albite, which is counterbalanced by their precipitation in the veins. The growth of phyllosilicates is enhanced in the vicinity of the veins. Textural observations point to all reactions occurring during the main deformation event.

The salinity of fluid inclusions in quartz veins that experienced 230-260°C is consistently lower than that of seawater, as a result of freshening of the fluid from smectite-to-illite transformation. At higher temperatures the salinity is closer or higher to the seawater. Crystallization of chlorite is a possible explanation for this salinity increase as chlorite requires additional water.

Observed mineral reactions, such as illite-to-chlorite transformation, affect the water budget in subducted sediments along the seismogenic zone where the pore fluid is transformed into crystal-bound water, potentially influencing the proportion of pore fluid and consequently pore fluid pressure.

Acknowledgments

The authors acknowledge support from LabEx VOLTAIRE (ANR-10-LABX-100-01) and EquipEx PLANEX (ANR-11-EQPX-0036) projects. J. Muñoz-Montecinos and two anonymous reviewers as well as S. Angiboust (editor) are thanked for their constructive comments and suggestions which helped to improve the manuscript. We thank S. Janiec for the preparation of thin sections, and to M. Soret, C. Herviou and L. Airaghi for fruitful discussions. Austin Gion is thanked for his help for correcting the English.

Literature:

Agard, P., Vidal, O., & Goffé, B. (2001). Interlayer and Si content of phengite in HP-LT carpholite-bearing metapelites: PHENGITE IN HP-LT METAPELITES. *Journal of Metamorphic Geology*, *19*(5), 479–495. https://doi.org/10.1046/j.0263-4929.2001.00322.x

Agard, P., Goffé, B., Touret, J. L. R., & Vidal, O. (2000). Retrograde mineral and fuid evolution in high-pressure metapelites (Schistes lustres unit, Western Alps). *Contributions to Mineralogy and Petrology*, *140*, 296–315.

Ahn, J. H., & Peacor, D. R. (1985). Transmision Electron Microscopy study of diagenetic chlorite in Gulf Coast argillaceous sediments. *Clay and Clay Minerals*, *33*(3), 228–236.

Angiboust, S., & Agard, P. (2010). Initial water budget: The key to detaching large volumes of eclogitized oceanic crust along the subduction channel? *Lithos*, *120*(3–4), 453–474. https://doi.org/10.1016/j.lithos.2010.09.007

Angiboust, S., Agard, P., Raimbourg, H., Yamato, P., & Huet, B. (2011). Subduction interface processes recorded by eclogite-facies shear zones (Monviso, W. Alps). *Lithos*, *127*(1–2), 222–238. https://doi.org/10.1016/j.lithos.2011.09.004

741 Angiboust, S., Pettke, T., De Hoog, J. C. M., Caron, B., & Oncken, O. (2014). Channelized Fluid Flow and
742 Eclogite-facies Metasomatism along the Subduction Shear Zone. *Journal of Petrology*, *55*(5),
743 883–916. https://doi.org/10.1093/petrology/egu010
744 Árkai, P., Faryad, S. W., Vidal, O., & Balogh, K. (2003). Very low-grade metamorphism of sedimentary
745 rocks of the Meliata unit, Western Carpathians, Slovakia: implications of phyllosilicate
746 characteristics. *International Journal of Earth Sciences*, *92*(1), 68–85.
747 https://doi.org/10.1007/s00531-002-0303-x
748 Audet, P., & Schwartz, S. Y. (2013). Hydrologic control of forearc strength and seismicity in the Costa
749 Rican subduction zone. *Nature Geoscience*, *6*(10), 852–855. https://doi.org/10.1038/ngeo1927
750 Battaglia, S. (2004). Variations in the chemical composition of illite from five geothermal fields: a
751 possible geothermometer. *Clay Minerals*, *39*(4), 501–510.
752 https://doi.org/10.1180/0009855043940150
753 Bebout, G. E. (1991). Field-Based Evidence for Devolatilization in Subduction Zones: Implications for Arc
754 Magmatism. *Science, New Series*, *251*(4992), 413–416.
755 Bebout, G. E., Agard, P., Kobayashi, K., Moriguti, T., & Nakamura, E. (2013). Devolatilization history and
756 trace element mobility in deeply subducted sedimentary rocks: Evidence from Western Alps
757 HP/UHP suites. *Chemical Geology*, *342*, 1–20. https://doi.org/10.1016/j.chemgeo.2013.01.009
758 Bebout, G. E., Ryan, J. G., & Leeman, W. P. (1993). B□Be systematics in subduction-related metamorphic
759 rocks: Characterization of the subducted component. *Geochimica et Cosmochimica Acta*, *57*(10),
760 2227–2237. https://doi.org/10.1016/0016-7037(93)90565-E
761 Becker, H., Jochum, K. P., & Carlson, R. W. (2000). Trace element fractionation during dehydration of
762 eclogites from high-pressure terranes and the implications for element fluxes in subduction
763 zones. *Chemical Geology*, *163*(1–4), 65–99. https://doi.org/10.1016/S0009-2541(99)00071-6

764 Beyssac, O., Goffé, B., Chopin, C., & Rouzaud, J. N. (2002). Raman spectra of carbonaceous material in
765 metasediments: a new geothermometer: RAMAN SPECTROSCOPY OF CARBONACEOUS
766 MATERIAL. *Journal of Metamorphic Geology*, *20*(9), 859–871. https://doi.org/10.1046/j.1525-
767 1314.2002.00408.x
768 Bodnar, R. J. (1993). Revised equation and table for determining the freezing point depression of H2O-
769 Nacl solutions. *Geochimica et Cosmochimica Acta*, *57*(3), 683–684.
770 https://doi.org/10.1016/0016-7037(93)90378-A
771 Boles, J. R., & Franks, S. G. (1979). Clay Diagenesis in Wilcox Sandstones of Southwest Texas:
772 Implications of Smectite Diagenesis on Sandstone Cementation, 16.
773 Bons, P. D., Elburg, M. A., & Gomez-Rivas, E. (2012). A review of the formation of tectonic veins and their
774 microstructures. *Journal of Structural Geology*, *43*, 33–62.
775 https://doi.org/10.1016/j.jsg.2012.07.005
776 Brantley, S. L., & Fisher, D. M. (1997). Segregation veins: evidence for the deformation and dewaterinf of
777 a low-grade metapelite. In *Deformation-enhanced Fluid Transport in the Earth's Crust and*
778 *Mantle* (pp. 267–288). Chapman & Hall, 2-6 Boundary Row, London SE1 8HN, UK.
779 Breeding, C. M., & Ague, J. J. (2002). Slab-derived fluids and quartz-vein formation in an accretionary
780 prism, Otago Schist, New Zealand. *Geology*, *30*(6), 499–502.
781 Byrne, T., & Fisher, D. M. (1990). Evidence for a Weak and Overpressured Decollement Beneath
782 Sediment-Dominated Accretionary Prisms. *Journal of Geophysical Research*, *95*(B6), 9081–9097.
783 Byrne, T. (1982). Structural evolution of coherent terranes in the Ghost Rocks Formation, Kodiak Island,
784 Alaska. *Geological Society, London, Special Publications*, *10*(1), 229–242.
785 https://doi.org/10.1144/GSL.SP.1982.010.01.15
786 Byrne, T., & Fisher, D. M. (1987). Episodic growth of the Kodiak convergent margin. *Nature*, *325*, 338–
787 341.

788 Caumon, M.-C., Dubessy, J., Robert, P., & Tarantola, A. (2014). Fused-silica capillary capsules (FSCCs) as
789 reference synthetic aqueous fluid inclusions to determine chlorinity by Raman spectroscopy.
790 *European Journal of Mineralogy*, *25*(5), 755–763. https://doi.org/10.1127/0935-
791 1221/2013/0025-2280
792 Caumon, M.-C., Tarantola, A., & Mosser-Ruck, R. (2015). Raman spectra of water in fluid inclusions: I.
793 Effect of host mineral birefringence on salinity measurement: Effect of mineral birefringence on
794 salinity measured by Raman spectroscopy. *Journal of Raman Spectroscopy*, *46*(10), 969–976.
795 https://doi.org/10.1002/jrs.4708
796 Colten-Bradley, V. A. (1987). Role of pressure in smectite dehydration; Effects on geopressure and
797 smectite- to-illite transformation. *American Association of Petroleum Geologists Bulletin*, *71*,
798 1414–1427.
799 Connelly, W. (1978). Uyak Complex, Kodiak Islands, Alaska: A Cretaceous subduction complex.
800 *Geological Society of America Bulletin*, *89*, 755–769.
801 Davis, D., Suppe, J., & Dahlen, F. A. (1983). Mechanics of fold-and-thrust belts and accretionary wedges.
802 *Journal of Geophysical Research*, *88*(B2), 1153. https://doi.org/10.1029/JB088iB02p01153
803 De Parseval, P., Amouric, M., Baronnet, A., Fortune, J.-P., Moine, B., & Ferret, J. (1994). HRTEM study of
804 the chloritization of micas in the talk-chlorite deposit at Trimouns (Pyrenees, France). *Eur. J.*
805 *Mineral*, *6*, 123–132.
806 Drief, A., & Nieto, F. (2000). Chemical composition of smectites formed in clastic sediments. Implications
807 for the smectite-illite transformation. *Clay Minerals*, *35*(4), 665–678.
808 https://doi.org/10.1180/000985500547124
809 Dubacq, B., Vidal, O., & De Andrade, V. (2010). Dehydration of dioctahedral aluminous phyllosilicates:
810 thermodynamic modelling and implications for thermobarometric estimates. *Contributions to*
811 *Mineralogy and Petrology*, *159*(2), 159–174. https://doi.org/10.1007/s00410-009-0421-6

812 Dubessy, J., Geisler, D., Kosztolanyi, C., & Vernet, M. (1983). The determination of sulphate in fluid
813 inclusions using the M.O.L.E. Raman microprobe. Application to a keuper halite and geochemical
814 consequences. *Geochimica et Cosmochimica Acta*, *47*(1), 1–10. https://doi.org/10.1016/0016-
815 7037(83)90086-8
816 Elliott, T. (2003). Tracers of the slab. In J. Eiler (Ed.), *Geophysical Monograph Series* (Vol. 138, pp. 23–45).
817 Washington, D. C.: American Geophysical Union. https://doi.org/10.1029/138GM03
818 Fagereng, Å., & Cooper, A. F. (2010). The metamorphic history of rocks buried, accreted and exhumed in
819 an accretionary prism: an example from the Otago Schist, New Zealand: METAMORPHIC
820 HISTORY OF AN ACCRETIONARY PRISM. *Journal of Metamorphic Geology*, *28*(9), 935–954.
821 https://doi.org/10.1111/j.1525-1314.2010.00900.x
822 Fagereng, Å., Remitti, F., & Sibson, R. H. (2011). Incrementally developed slickenfibers — Geological
823 record of repeating low stress-drop seismic events? *Tectonophysics*, *510*(3–4), 381–386.
824 https://doi.org/10.1016/j.tecto.2011.08.015
825 Fagereng, Å., Diener, J. F. A., Ellis, S., & Remitti, F. (2018). Fluid-related deformation processes at the up-
826 and downdip limits of the subduction thrust seismogenic zone: What do the rocks tell us? In
827 Timothy Byrne, M. B. Underwood, D. Fisher, L. McNeill, D. Saffer, K. Ujiie, & A. Yamaguchi,
828 *Geology and Tectonics of Subduction Zones: A Tribute to Gaku Kimura*. Geological Society of
829 America. https://doi.org/10.1130/2018.2534(12)
830 Ferrill, D. A., Morris, A. P., Evans, M. A., Burkhard, M., Groshong, R. H., & Onasch, C. M. (2004). Calcite
831 twin morphology: a low-temperature deformation geothermometer. *Journal of Structural*
832 *Geology*, *26*(8), 1521–1529. https://doi.org/10.1016/j.jsg.2003.11.028
833 Ferry, J. M. (1981). Petrology of graphitic sulfide-rich schists from south-central Maine: an example of
834 desulfidation during prograde regional methamorphism. *American Mineralogist*, *66*, 908–930.

Fisher, D. M., & Byrne, T. (1987). Structural evolution of underthrusted sediments, Kodiak Islands, Alaska. *Tectonics*, *6*(6), 775–793. https://doi.org/10.1029/TC006i006p00775

Fisher, D. M., & Byrne, T. (1990). The character and distribution of mineralized fractures in the Kodiak Formation, Alaska: Implications for fluid flow in an underthrust sequence. *Journal of Geophysical Research*, *95*(B6), 9069. https://doi.org/10.1029/JB095iB06p09069

Fisher, D. M., & Brantley, S. L. (1992). Models of quartz overgrowth and vein formation: Deformation and episodic fluid flow in an ancient subduction zone. *Journal of Geophysical Research*, *97*(B13), 20043. https://doi.org/10.1029/92JB01582

Fisher, D. M., & Brantley, S. L. (2014). The role of silica redistribution in the evolution of slip instabilities along subduction interfaces: Constraints from the Kodiak accretionary complex, Alaska. *Journal of Structural Geology*, *69*, 395–414. https://doi.org/10.1016/j.jsg.2014.03.010

Fisher, D. M., & Byrne, T. (1992). Strain variations in an ancient accretionary complex: Implications for forearc evolution. *Tectonics*, *11*(2), 330–347. https://doi.org/10.1029/91TC01490

Fisher, D. M., Brantley, S. L., Everett, M., & Dzvonik, J. (1995). Cyclic fluid flow through a regionally extensive fracture network within the Kodiak accretionary prism. *Journal of Geophysical Research: Solid Earth*, *100*(B7), 12881–12894. https://doi.org/10.1029/94JB02816

Frey, M. (1978). Progressive Low-Grade Metamorphism of a Black Shale Formation, Central Swiss Alps, with Special Reference to Pyrophyllite and Margarite Bearing Assemblages. *Journal of Petrology*, *19*(1), 95–135. https://doi.org/10.1093/petrology/19.1.95

Frey, M., Bucher, K., & Frank, E. (1980). Alpine metamorphism along the geotraverse Basel-Chiasso : a review. https://doi.org/10.5169/SEALS-164971

Goffé, B., & Chopin, C. (1986). High-pressure metamorphism in the Western Alps : zoneography of metapelites, chronology and consequences. https://doi.org/10.5169/SEALS-50880

858 Hacker, B. R. (2008). H2O subduction beyond arcs. *Geochemistry, Geophysics, Geosystems*, *9*(3), n/a-n/a.
859 https://doi.org/10.1029/2007GC001707
860 Hacker, B. R., Abers, G. A., & Peacock, S. M. (2003). Subduction factory 1. Theoretical mineralogy,
861 densities, seismic wave speeds, and H $_2$ O contents: SUBDUCTION ZONE MINERALOGY AND
862 PHYSICAL PROPERTIES. *Journal of Geophysical Research: Solid Earth*, *108*(B1).
863 https://doi.org/10.1029/2001JB001127
864 Hall, A. J. (1986). Pyrite-pyrrhotine redox reactions in nature. *Mineralogical Magazine*, *50*(356), 223–
865 229. https://doi.org/10.1180/minmag.1986.050.356.05
866 Herviou, C., & Bonnet, G. (2023). Paleocene-Eocene high-pressure carbonation of Western Alps
867 serpentinites: positive feedback between deformation and CO2-CH4 fluid ingression responsible
868 for slab slicing? *Geochemistry, Geophysics, Geosystems*.
869 Herviou, C., Verlaguet, A., Agard, P., Locatelli, M., Raimbourg, H., Lefeuvre, B., & Dubacq, B. (2021).
870 Along-dip variations of subduction fluids: The 30–80 km depth traverse of the Schistes Lustrés
871 complex (Queyras-Monviso, W. Alps). *Lithos*, *394–395*, 106168.
872 https://doi.org/10.1016/j.lithos.2021.106168
873 Hower, J., Eslinger, E. V., Hower, M. E., & Perry, E. A. (1976). Mechanism of burial metamorphism of
874 argillaceous sediment: 1. Mineralogical and chemical evidence. *Geological Society of America*
875 *Bulletin*, *87*(5), 725. https://doi.org/10.1130/0016-7606(1976)87<725:MOBMOA>2.0.CO;2
876 Hyndman, R. D., & Wang, K. (1993). Thermal constraints on the zone of major thrust earthquake failure:
877 The Cascadia Subduction Zone. *Journal of Geophysical Research: Solid Earth*, *98*(B2), 2039–2060.
878 https://doi.org/10.1029/92JB02279
879 Jarrard, R. D. (2003). Subduction fluxes of water, carbon dioxide, chlorine, and potassium: SUBDUCTION
880 FLUXES OF WATER. *Geochemistry, Geophysics, Geosystems*, *4*(5), n/a-n/a.
881 https://doi.org/10.1029/2002GC000392

Kameda, J., Raimbourg, H., Kogure, T., & Kimura, G. (2011a). Low-grade metamorphism around the down-dip limit of seismogenic subduction zones: Example from an ancient accretionary complex in the Shimanto Belt, Japan. *Tectonophysics*, *502*(3–4), 383–392. https://doi.org/10.1016/j.tecto.2011.02.010

Kameda, J., Yamaguchi, A., Saito, S., Sakuma, H., Kawamura, K., & Kimura, G. (2011b). A new source of water in seismogenic subduction zones: A SOURCE OF WATER IN SEISMOGENIC ZONE. *Geophysical Research Letters*, *38*(22), n/a-n/a. https://doi.org/10.1029/2011GL048883

Kastner, M. (1981). Authigenic silicates in deep-sea sediments: formation and diagenesis. In *The oceanic lithosphere The sea* (C. Emiliani, Vol. 7, pp. 915–980). Wiley.

Kastner, M., Solomon, E. A., Harris, R. N., & Torres, M. E. (2014). Fluid Origins, Thermal Regimes, and Fluid and Solute Fluxes in the Forearc of Subduction Zones. In *Developments in Marine Geology* (Vol. 7, pp. 671–733). Elsevier. https://doi.org/10.1016/B978-0-444-62617-2.00022-0

Kawabata, K., Tanaka, H., & Kimura, G. (2007). Mass transfer and pressure solution in deformed shale of accretionary complex: Examples from the Shimanto Belt, southwestern Japan. *Journal of Structural Geology*, *29*(4), 697–711. https://doi.org/10.1016/j.jsg.2006.11.009

van Keken, P. E., Kiefer, B., & Peacock, S. M. (2002). High-resolution models of subduction zones: Implications for mineral dehydration reactions and the transport of water into the deep mantle: HIGH-RESOLUTION MODELS OF SUBDUCTION ZONES. *Geochemistry, Geophysics, Geosystems*, *3*(10), 1 of 20–20 20. https://doi.org/10.1029/2001GC000256

Kominz, M. A., & Pekar, S. F. (2001). Oligocene eustasy from two-dimensional sequence stratigraphic backstripping. *Geological Society of America Bulletin*, *113*(3), 291–304. https://doi.org/10.1130/0016-7606(2001)113<0291:OEFTDS>2.0.CO;2

Komninou, A., & Sverjensky, D. A. (1995). Pre-ore hydrothermal alteration in an unconformity-type uranium deposit. *Contributions to Mineralogy and Petrology*, *121*(1), 99–114. https://doi.org/10.1007/s004100050092

Kondo, H., Kimura, G., Masago, H., Ohmori-Ikehara, K., Kitamura, Y., Ikesawa, E., et al. (2005). Deformation and fluid flow of a major out-of-sequence thrust located at seismogenic depth in an accretionary complex: Nobeoka Thrust in the Shimanto Belt, Kyushu, Japan: NOBEOKA THRUST, A SEISMOGENIC OST. *Tectonics*, *24*(6), n/a-n/a. https://doi.org/10.1029/2004TC001655

Kontak, D. J. (2004). Analysis of evaporate mounds as a compement to fluid-inclusion thermometric data: Case studies from granitic environments in Nova Scotia and Peru. *THE CANADIAN MINERALOGIST*, 16.

Lahfid, A., Beyssac, O., Deville, E., Negro, F., Chopin, C., & Goffé, B. (2010). Evolution of the Raman spectrum of carbonaceous material in low-grade metasediments of the Glarus Alps (Switzerland): RSCM in low-grade metasediments. *Terra Nova*, *22*(5), 354–360. https://doi.org/10.1111/j.1365-3121.2010.00956.x

Lanari, P., Vidal, O., De Andrade, V., Dubacq, B., Lewin, E., Grosch, E. G., & Schwartz, S. (2014). XMapTools: A MATLAB©-based program for electron microprobe X-ray image processing and geothermobarometry. *Computers & Geosciences*, *62*, 227–240. https://doi.org/10.1016/j.cageo.2013.08.010

Lefeuvre, B., Agard, P., Verlaguet, A., Dubacq, B., & Plunder, A. (2020). Massive formation of lawsonite in subducted sediments from the Schistes Lustrés (W. Alps): Implications for mass transfer and decarbonation in cold subduction zones. *Lithos*, *370–371*, 105629. https://doi.org/10.1016/j.lithos.2020.105629

926 Majzlan, J., Grevel, K.-D., & Navrotsky, A. (2003). Thermodynamics of Fe oxides: Part II. Enthalpies of
927 formation and relative stability of goethite (a-FeOOH), lepidocrocite (g-FeOOH), and maghemite
928 (g-Fe2O3). *American Mineralogist*, *88*(5–6), 855–859. https://doi.org/10.2138/am-2003-5-614
929 Makvandi, S., Huang, X., Beaudoin, G., Quirt, D., Ledru, P., & Fayek, M. (2021). Trace element signatures
930 in hematite and goethite associated with the Kiggavik–Andrew Lake structural trend U deposits
931 (Nunavut, Canada). *Mineralium Deposita*, *56*(3), 509–535. https://doi.org/10.1007/s00126-020-
932 00980-y
933 Masci, L., Dubacq, B., Verlaguet, A., Chopin, C., De Andrade, V., & Herviou, C. (2019). A XANES and EPMA
934 study of Fe3+ in chlorite: Importance of oxychlorite and implications for cation site distribution
935 and thermobarometry. *American Mineralogist*, *104*(3), 403–417. https://doi.org/10.2138/am-
936 2019-6766
937 Moore, J. C., & Vrolijk, P. (1992). Fluids in accretionary prisms. *Reviews of Geophysics*, *30*(2), 113.
938 https://doi.org/10.1029/92RG00201
939 Moore, J. C., Byrne, T., Plumley, P. W., Reid, M., Gibbons, H., & Coe, R. S. (1983). Paleogene evolution of
940 the Kodiak 266 Islands, Alaska: Consequences of ridge-trench interaction in a more southerly
941 latitude. *Tectonics*, *2*, 265–293.
942 Muffler, L. J. P., & White, D. F. (1969). Active Metamorphism of Upper Cenozoic Sediments in the Salton
943 Sea Geothermal Field and the Salton Trough, Southeastern California. *Geological Society of*
944 *America Bulletin*, *80*, 157–182.
945 Mullis, J., Dubessy, J., Poty, B., & O'Neil, J. (1994). Fluid regimes during late stages of a continental
946 collision: Physical, chemical, and stable isotope measurements of fluid inclusions in fissure
947 quartz from a geotraverse through the Central Alps, Switzerland. *Geochimica et Cosmochimica*
948 *Acta*, *58*(10), 2239–2267. https://doi.org/10.1016/0016-7037(94)90008-6

949 Muñoz-Montecinos, J., Angiboust, S., & Garcia-Casco, A. (2021). Blueschist-facies paleo-earthquakes in a
950 serpentinite channel (Zagros suture, Iran) enlighten seismogenesis in Mariana-type subduction
951 margins. *Earth and Planetary Science Letters*, *573*, 117135.
952 https://doi.org/10.1016/j.epsl.2021.117135
953 Muñoz-Montecinos, J., Angiboust, S., Garcia-Casco, A., Glodny, J., & Bebout, G. (2021). Episodic
954 hydrofracturing and large-scale flushing along deep subduction interfaces: Implications for fluid
955 transfer and carbon recycling (Zagros Orogen, southeastern Iran). *Chemical Geology*, *571*,
956 120173. https://doi.org/10.1016/j.chemgeo.2021.120173
957 Nishi, H. (1988). Structural analysis of the Shimanto Accretionary Complex, Kyushu, Japan, based on
958 foraminiferal biostratigraphy. *Tectonics*, *7*(3), 641–652.
959 https://doi.org/10.1029/TC007i003p00641
960 Nishiyama, N., Ujiie, K., & Kano, M. (2021). Spatial changes in inclusion band spacing as an indicator of
961 temporal changes in slow slip and tremor recurrence intervals. *Earth, Planets and Space*, *73*(1),
962 126. https://doi.org/10.1186/s40623-021-01448-7
963 Oleskevich, D. A., Hyndman, R. D., & Wang, K. (1999). The updip and downdip limits to great subduction
964 earthquakes: Thermal and structural models of Cascadia, south Alaska, SW Japan, and Chile.
965 *Journal of Geophysical Research: Solid Earth*, *104*(B7), 14965–14991.
966 https://doi.org/10.1029/1999JB900060
967 Palazzin, G., Raimbourg, H., Famin, V., Jolivet, L., Kusaba, Y., & Yamaguchi, A. (2016). Deformation
968 processes at the down-dip limit of the seismogenic zone: The example of Shimanto accretionary
969 complex. *Tectonophysics*, *687*, 28–43. https://doi.org/10.1016/j.tecto.2016.08.013
970 Peacock, S. M. (1993). The importance of blueschist → eclogite dehydration reactions in subducting
971 oceanic crust. *Geological Society of America Bulletin*, *105*(5), 684–694.
972 https://doi.org/10.1130/0016-7606(1993)105<0684:TIOBED>2.3.CO;2

973 Penniston-Dorland, S. C., Bebout, G. E., Pogge von Strandmann, P. A. E., Elliott, T., & Sorensen, S. S.
974 (2012). Lithium and its isotopes as tracers of subduction zone fluids and metasomatic processes:
975 Evidence from the Catalina Schist, California, USA. *Geochimica et Cosmochimica Acta*, *77*, 530–
976 545. https://doi.org/10.1016/j.gca.2011.10.038
977 Perry, E. A., & Hower, J. (1970). Burial diagenesis in Gulf Coast pelitic sediments. *Clays Clay Minerals*, *18*,
978 165–177.
979 Plafker, G., Moore, J. C., Winkler, G. R., & Berg, H. (1994). Geology of the southern Alaska margin. *The*
980 *Geology of 249 Alaska: Boulder, Colorado, Geological Society of America, Geology of North*
981 *America*, *1*, 389–449.
982 Plank, T. (2014). The Chemical Composition of Subducting Sediments. In *Treatise on Geochemistry* (pp.
983 607–629). Elsevier. https://doi.org/10.1016/B978-0-08-095975-7.00319-3
984 Plunder, A., Agard, P., Dubacq, B., Chopin, C., & Bellanger, M. (2012). How continuous and precise is the
985 record of P-T paths? Insights from combined thermobarometry and thermodynamic modelling
986 into subduction dynamics (Schistes Lustrés, W. Alps): TOWARDS Continuous P-T PATHS? *Journal*
987 *of Metamorphic Geology*, *30*(3), 323–346. https://doi.org/10.1111/j.1525-1314.2011.00969.x
988 Rahn, M., Mullis, J., Erdelbrock, K., & Frey, M. (1994). Very low-grade metamorphism of the Taveyanne
989 greywacke, Glarus Alps, Switzerland. *Journal of Metamorphic Geology*, *12*(5), 625–641.
990 https://doi.org/10.1111/j.1525-1314.1994.tb00047.x
991 Raimbourg, H. (2015). Fluid circulation in the depths of accretionary prisms: an example of the Shimanto
992 Belt, Kyushu, Japan, 16.
993 Raimbourg, H., Tadahiro, S., Asuka, Y., Haruka, Y., & Kimura, G. (2009). Horizontal shortening versus
994 vertical loading in accretionary prisms: ACCRETIONARY PRISM STRESS CONDITIONS.
995 *Geochemistry, Geophysics, Geosystems*, *10*(4), n/a-n/a. https://doi.org/10.1029/2008GC002279

Raimbourg, H., Augier, R., Famin, V., Gadenne, L., Palazzin, G., Yamaguchi, A., & Kimura, G. (2014). Long-term evolution of an accretionary prism: The case study of the Shimanto Belt, Kyushu, Japan: Long-term evolution of the Shimanto Belt. *Tectonics*, *33*(6), 936–959. https://doi.org/10.1002/2013TC003412

Raimbourg, H., Famin, V., Palazzin, G., Yamaguchi, A., & Augier, R. (2017). Tertiary evolution of the Shimanto belt (Japan): A large-scale collision in Early Miocene: Early Miocene Collision in Shimanto Belt. *Tectonics*, *36*(7), 1317–1337. https://doi.org/10.1002/2017TC004529

Raimbourg, H., Famin, V., Palazzin, G., Mayoux, M., Jolivet, L., Ramboz, C., & Yamaguchi, A. (2018). Fluid properties and dynamics along the seismogenic plate interface. *Geosphere*, *14*(2), 469–491. https://doi.org/10.1130/GES01504.1

Raimbourg, H., Rajič, K., Moris-Muttoni, B., Famin, V., Palazzin, G., Fisher, D. M., et al. (2021). Quartz vein geochemistry records deformation processes in convergent zones. *Geochemistry, Geophysics, Geosystems*, *22*. https://doi.org/10.1029/2020GC009201

Ramirez, G., Smye, A., Fisher, D. M., Hashimoto, Y., & Yamaguchi, A. (2021). Constraints on Element Mobility During Deformation Within the Seismogenic Zone, Shimanto Belt, Japan. *Geochemistry, Geophysics, Geosystems*, *22*(8). https://doi.org/10.1029/2020GC009594

Rauchenstein-Martinek, K., Wagner, T., Wälle, M., Heinrich, C. A., & Arlt, T. (2016). Chemical evolution of metamorphic fluids in the Central Alps, Switzerland: insight from LA-ICPMS analysis of fluid inclusions. *Geofluids*, *16*(5), 877–908. https://doi.org/10.1111/gfl.12194

Reynard, B. (2013). Serpentine in active subduction zones. *Lithos*, *178*, 171–185. https://doi.org/10.1016/j.lithos.2012.10.012

Rietveld, H. M. (1969). A profile refinement method for nuclear and magnetic structures. *Journal of Applied Crystallography*, *2*(2), 65–71. https://doi.org/10.1107/S0021889869006558

Rowe, C. D., Meneghini, F., & Moore, J. C. (2009). Fluid-rich damage zone of an ancient out-of-sequence thrust, Kodiak Islands, Alaska: DAMAGE ZONE OF ANCIENT OOST. *Tectonics*, *28*(1), n/a-n/a. https://doi.org/10.1029/2007TC002126

Rupke, L. (2004). Serpentine and the subduction zone water cycle. *Earth and Planetary Science Letters*, *223*(1–2), 17–34. https://doi.org/10.1016/j.epsl.2004.04.018

Saffer, D. M., & Tobin, H. J. (2011). Hydrogeology and Mechanics of Subduction Zone Forearcs: Fluid Flow and Pore Pressure. *Annual Review of Earth and Planetary Sciences*, *39*(1), 157–186. https://doi.org/10.1146/annurev-earth-040610-133408

Saffer, D. M., Lockner, D. A., & McKiernan, A. (2012). Effects of smectite to illite transformation on the frictional strength and sliding stability of intact marine mudstones: FRICTION AND SMECTITE TRANSFORMATION. *Geophysical Research Letters*, *39*(11), n/a-n/a. https://doi.org/10.1029/2012GL051761

Saito, M. (1996). Geological Map of Japan, 1:50,000. Geol. Surv. Jpn., Shiibamura.

Sakaguchi, A. (1999). Thermal maturity in the Shimanto accretionary prism, southwest Japan, with the thermal change of the subducting slab: fluid inclusion and vitrinite reflectance study. *Earth and Planetary Science Letters*, *173*(1–2), 61–74. https://doi.org/10.1016/S0012-821X(99)00219-8

Sakai et al., T. (1984). Microfossil stratigraphy of the Paleogene System in Kyushu Shimanto Belt. *Biostratigraphy and International Correlation of the Paleogene System in Japan*, 95–112.

Sample, J. C., & Fisher, D. M. (1986). Duplex accretion and underplating in an ancient accretionary prism, Kodiak Islands, Alaska. *Geology*, *14*, 160–163.

Sample, J. C., & Moore, J. C. (1987). Structural style and kinematics of an underplated slate belt, Kodiak and adjacent 260 islands, Alaska. *Geological Society of America Bulletin*, *99*, 7–20.

1041 Scambelluri, M., Fiebig, J., Malaspina, N., Müntener, O., & Pettke, T. (2004). Serpentinite Subduction:
1042 Implications for Fluid Processes and Trace-Element Recycling. *International Geology Review*,
1043 *46*(7), 595–613. https://doi.org/10.2747/0020-6814.46.7.595
1044 Scambelluri, M., Pettke, T., & Cannaò, E. (2015). Fluid-related inclusions in Alpine high-pressure
1045 peridotite reveal trace element recycling during subduction-zone dehydration of serpentinized
1046 mantle (Cima di Gagnone, Swiss Alps). *Earth and Planetary Science Letters*, *429*, 45–59.
1047 https://doi.org/10.1016/j.epsl.2015.07.060
1048 Schmidt, D., Schmidt, S. T., Mullis, J., Ferreiro Mählmann, R., & Frey, M. (1997). Very low grade
1049 metamorphism of the Taveyanne formation of western Switzerland. *Contributions to Mineralogy*
1050 *and Petrology*, *129*(4), 385–403. https://doi.org/10.1007/s004100050344
1051 Schmidt, M. W., & Poli, S. (2014). Devolatilization During Subduction. In *Treatise on Geochemistry* (pp.
1052 669–701). Elsevier. https://doi.org/10.1016/B978-0-08-095975-7.00321-1
1053 Schneider, C. A., Rasband, W. S., & Eliceiri, K. W. (2012). NIH Image to ImageJ: 25 years of image
1054 analysis. *Nature Methods*, *9*(7), 671–675. https://doi.org/10.1038/nmeth.2089
1055 Sharp, Z. D., & Kirschner, D. L. (1994). Quartz-calcite oxygen isotope thermometry: A calibration based
1056 on natural isotopic variations. *Geochimica et Cosmochimica Acta*, *58*(20), 4491–4501.
1057 https://doi.org/10.1016/0016-7037(94)90350-6
1058 Simons, K. K., Harlow, G. E., Brueckner, H. K., Goldstein, S. L., Sorensen, S. S., Hemming, N. G., &
1059 Langmuir, C. H. (2010). Lithium isotopes in Guatemalan and Franciscan HP–LT rocks: Insights into
1060 the role of sediment-derived fluids during subduction. *Geochimica et Cosmochimica Acta*,
1061 *74*(12), 3621–3641. https://doi.org/10.1016/j.gca.2010.02.033
1062 Spandler, C., & Pirard, C. (2013). Element recycling from subducting slabs to arc crust: A review. *Lithos*,
1063 *170–171*, 208–223. https://doi.org/10.1016/j.lithos.2013.02.016

1064 Spandler, C., Hermann, J., Arculus, R., & Mavrogenes, J. (2003). Redistribution of trace elements during
1065 prograde metamorphism from lawsonite blueschist to eclogite facies; implications for deep
1066 subduction-zone processes. *Contributions to Mineralogy and Petrology*, *146*(2), 205–222.
1067 https://doi.org/10.1007/s00410-003-0495-5
1068 Spinelli, G. A. (2004). Along-strike variations in underthrust sediment dewatering on the Nicoya margin,
1069 Costa Rica related to the updip limit of seismicity. *Geophysical Research Letters*, *31*(4), L04613.
1070 https://doi.org/10.1029/2003GL018863
1071 Stern, C. R. (2011). Subduction erosion: Rates, mechanisms, and its role in arc magmatism and the
1072 evolution of the continental crust and mantle. *Gondwana Research*, *20*(2–3), 284–308.
1073 https://doi.org/10.1016/j.gr.2011.03.006
1074 Stern, R. J. (2002). SUBDUCTION ZONES: SUBDUCTION ZONES. *Reviews of Geophysics*, *40*(4), 3-1-3–38.
1075 https://doi.org/10.1029/2001RG000108
1076 Sun, Q., Zhao, L., Li, N., & Liu, J. (2010). Raman spectroscopic study for the determination of Cl−
1077 concentration (molarity scale) in aqueous solutions: Application to fluid inclusions. *Chemical*
1078 *Geology*, *272*(1–4), 55–61. https://doi.org/10.1016/j.chemgeo.2010.02.004
1079 Taetz, S., John, T., Bröcker, M., & Spandler, C. (2016). Fluid–rock interaction and evolution of a high-
1080 pressure/low-temperature vein system in eclogite from New Caledonia: insights into intraslab
1081 fluid flow processes. *Contributions to Mineralogy and Petrology*, *171*(11), 90.
1082 https://doi.org/10.1007/s00410-016-1295-z
1083 Tarantola, A., Mullis, J., Vennemann, T., Dubessy, J., & de Capitani, C. (2007). Oxidation of methane at
1084 the CH4/H2O–(CO2) transition zone in the external part of the Central Alps, Switzerland:
1085 Evidence from stable isotope investigations. *Chemical Geology*, *237*(3–4), 329–357.
1086 https://doi.org/10.1016/j.chemgeo.2006.07.007

1087 Tarantola, A., Mullis, J., Guillaume, D., Dubessy, J., de Capitani, C., & Abdelmoula, M. (2009). Oxidation
1088 of CH4 to CO2 and H2O by chloritization of detrital biotite at 270±5 °C in the external part of the
1089 Central Alps, Switzerland. *Lithos*, *112*(3–4), 497–510.
1090 https://doi.org/10.1016/j.lithos.2009.04.008
1091 Taylor, J., & Clapp, R. (1991). New Features and Advanced Applications of Siroquant: A Personal
1092 Computer XRD Full Profile Quantitative Analysis Software Package. *Advances in X-Ray Analysis*,
1093 *35(A)*, 49–55. https://doi.org/doi:10.1154/S037603080000865X
1094 Teraoka, Y., & Okumura, K. (1992). Tectonic division and Cretaceous sandstone compositions of the
1095 Northern Belt of the Shimanto Terrane, southwest Japan. *Mem. Geol. Soc. Jpn.*, *38*, 261–270.
1096 Toriumi, M., & Teruya, J. (1988). Tectono-metamorphism of the Shimanto Belt. *Modern Geology*, *12*,
1097 303–324.
1098 Ujiie, K., Saishu, H., Fagereng, Å., Nishiyama, N., Otsubo, M., Masuyama, H., & Kagi, H. (2018). An
1099 Explanation of Episodic Tremor and Slow Slip Constrained by Crack-Seal Veins and Viscous Shear
1100 in Subduction Mélange. *Geophysical Research Letters*, *45*(11), 5371–5379.
1101 https://doi.org/10.1029/2018GL078374
1102 Vannucchi, P. (2019). Scaly fabric and slip within fault zones. *Geosphere*, *15*(2), 342–356.
1103 https://doi.org/10.1130/GES01651.1
1104 Velde, B. (1985). *Clay Minerals: a Physico-chemical Explanation of their Occurrence*. Elsevier.
1105 Vidal, O., & Parra, T. (2000). Exhumation paths of high-pressure metapelites obtained from local
1106 equilibria for chlorite-phengite assemblages. *Geological Journal*, *35*(3–4), 139–161.
1107 https://doi.org/10.1002/gj.856
1108 Vidal, O., De Andrade, V., Lewin, E., Munoz, M., Parra, T., & Pascarelli, S. (2006). P-T-deformation-
1109 Fe3+/Fe2+ mapping at the thin section scale and comparison with XANES mapping: application
1110 to a garnet-bearing metapelite from the Sambagawa metamorphic belt (Japan): P-T-

DEFORMATION-FE3+/FE2+ MAPPING. *Journal of Metamorphic Geology*, *24*(7), 669–683. https://doi.org/10.1111/j.1525-1314.2006.00661.x

Vrolijk, P., Myers, G., & Moore, J. C. (1988). Warm fluid migration along tectonic melanges in the Kodiak Accretionary Complex, Alaska. *Journal of Geophysical Research: Solid Earth*, *93*(B9), 10313–10324. https://doi.org/10.1029/JB093iB09p10313

Wang, H. (1996). Diagenesis and Metamorphism of Clay Minerals in the Helvetic Alps of Eastern Switzerland. *Clays and Clay Minerals*, *44*(1), 96–112. https://doi.org/10.1346/CCMN.1996.0440109

Yoshida, K., Hirajima, T., Ohsawa, S., Kobayashi, T., Mishima, T., & Sengen, Y. (2015). Geochemical features and relative B–Li–Cl compositions of deep-origin fluids trapped in high-pressure metamorphic rocks. *Lithos*, *226*, 50–64. https://doi.org/10.1016/j.lithos.2015.03.002

Zane, A., Sassi, A., & Guidotti, C. V. (1998). New Data On Metamorphic Chlorite As A Petrogenetic Indicator Mineral, With Special Regard To Greenschist-Facies Rocks. *THE CANADIAN MINERALOGIST*, *36*, 713–726.

FIGURE CAPTIONS

Figure 1. Geological map of (a) the Kodiak accretionary complex, Alaska, and (b) the Shimanto Belt on Kyushu, Japan, with the locations of samples used in this study.

Figure 2. Field pictures of metasediments and veins used in this study from the Kodiak accretionary complex (a and c) and from the Shimanto Belt (b and d). (a) Mode 1 quartz veins in coherent portion of the Kodiak Landward Belt (Alaska). Note that veins are restricted to sandstone/siltstone layers and absent in mudstone. (b) Photograph of a polished rock slab from the Hyuga Tectonic Mélange (Shimanto Belt, Japan). Quartz veins are located in the sandstone lenses in strongly sheared shales. (c) Top-to-the-NW shear veins in shale-dominated zone cutting across the foliation S_1, Kodiak Central Belt. (d) Example of en echelon vein arrays in shale-rich zone of the Foliated Morotsuka (Shimanto Belt, Japan). Blue arrows point to the sampled veins, whereas red arrows indicate shear bands and displacement directions.

Figure 3. (a) Example of a H_2O Raman spectrum from fluid inclusion, decomposed into two Gaussian bands. (b) Calculated K' value from the standard solutions with known Cl^- molarity. (c) Salinity of 22 fluid inclusions estimated by Raman spectroscopy and microthermometry, showing the good agreement between the two independent measurements.

Figure 4. Representative Raman spectra of carbonaceous material from (a) the Kodiak Landward Belt and (b) the Kodiak Central Belt. The spectra were deconvoluted following the method of Lahfid et al. (2010).

Figure 5. Main microstructures and mineral phases in lower- and higher-grade samples of the Kodiak accretionary complex and the Shimanto Belt: (a) Photomicrograph of intercalated quartz ribbons and pelitic matrix rich in fine-grained phyllosilicates, plagioclase and quartz (Sample HN299C, Shimanto). (b) SEM-BSE image showing intertwined illite and chlorite (sample KO17E, Kodiak). (c) Photomicrograph (cross-polarized view) of chlorite shear band at low angle to the main foliation (Sample HN299A, Shimanto). (d) SEM-BSE image of a pelitic matrix with scaly fabrics enriched in Ti-oxides and sulfides (Sample HN299A, Shimanto). (e) Photomicrograph and (f) SEM-BSE image of the contact between a shear vein and the surrounding matrix. Note the rim of increasing crystal size in the matrix in immediate contact with the vein compared to the host rock further away (sample KO38, Kodiak). (g) Optical photomicrograph (left: plain-polarized view; right: cross-polarized view) of illite+chlorite layers separated by scaly fabrics (Sample HN285, Shimanto). (h) BSE image of strongly foliated metapelite with the alignment of plagioclase and quartz parallel to the foliation (Sample HN247, Shimanto). (i) SEM-BSE image and (j) A mask image of EDS Ti and Fe maps of a shear zone enriched in titanium and iron (Sample HN145, Shimanto). Abbreviations: Qz – quartz; Pl – plagioclase; Chl – chlorite; Ilt – illite; Ap – apatite.

Figure 6. Characteristic vein textures in lower- and higher-grade samples: (a) A Mode-1 quartz-calcite vein with blocky and elongated quartz. (b) Elongated quartz with trails of pseudo-secondary fluid inclusions perpendicular to the stretching direction. (c) A sample slab with two extensional shear veins (Sample KO33C, Kodiak). (d) Deformed calcite in shear vein. (e) A part of shear vein characterized by crack-seal texture. (f) SEM-BSE image (left) and mask image (right) of an extensional vein connected to a shear vein from (c), showing chlorite rim along the contact between vein and matrix. Note albite crystals in the vein and its absence in the matrix.

Figure 7. (a) A field photo of an example of quartz vein with veinlets only on the northwestern side (Site KO30, Kodiak). (b) Scan of the thin section from the vein of Fig. 7a. (c) SEM-BSE image of the host rock closer to the vein characterized by the presence of a foliation (S_1) and a crenulation cleavage (S_2), whereas

away from the vein (d) only the foliation (S_1) is present. (e-f) Mask images of (c-d). Note that away from the vein quartz is still present in the host rock, whereas closer to the vein it is completely absent. (g-h) Mask images of Ti- and Ca- bearing phases: titanite, anatase and apatite. In zones showing crenulation cleavage, titanite is partly dissolved and anatase precipitates as indicated by white arrows, whereas titanite is still present in the host rock away from the vein.

Figure 8. Major and minor element results analyzed by X-ray fluorescence normalized by TiO_2 versus peak-metamorphic temperature. SO_3 and LOI are plotted without normalization.

Figure 9. Chemical composition of illite and chlorite: Si^{IV} (apfu) in illite versus (a) total alkali (apfu) and (b) magnesium number (X_{Mg}). Si apfu in chlorite versus (c) sum at octahedral position and (d) magnesium number (X_{Mg} = $Mg^{2+}/(Fe^{2+}+Mg^{2+})$). (e) Composition of phyllosilicates shown in ternary diagram Si/4 – (Na+K+2Ca) – ($Mg+Fe^{2+}$) according to Velde (1985). (f) Composition of chlorite in amesite (Am) – sudoite (Sud) – clinochlore+daphnite (Clin+Daph) ternary diagram.

Figure 10. Examples of illite-chlorite equilibrium calculations in samples from (a) the Kodiak Central Belt (KO38, Kodiak) and (b) the Foliated Morotsuka (HN285, Shimanto). Bold lines represent independent reactions: (1) $(PrlH)_{Phg} = (Prl)_{Phg} + H_2O$; (2) 4 Qtz - $(Mg\text{-}Am)_{Chl}$ = 2 $(PrlH)_{Phg}$ + 2 $(Sud)_{Chl}$; (3) - 2 $(Mg\text{-}Cel)_{Phg}$ + 15 Qtz + 2 $(Ms)_{Phg}$ = 4 $(Prl)_{Phg}$ + $(Sud)_{Chl}$; (4) - 5 $(Mg\text{-}Cel)_{Phg}$ + $(Clin)_{Chl}$ = $(Fe\text{-}Am)_{Chl}$ + 4 $(Fe\text{-}Cel)_{Phg}$ + $(Ms)_{Phg}$; (5) - 4 $(Mg\text{-}Cel)_{Phg}$ + 4 $(Daph)_{Chl}$ = 5 $(Fe\text{-}Am)_{Chl}$ + $(Mg\text{-}Am)_{Chl}$ + 4 $(Ms)_{Phg}$; (6) 4 $(Mg\text{-}Cel)_{Phg}$ + $(Daph)_{Chl}$ = 5 $(Fe\text{-}Cel)_{Phg}$ - $(Mg\text{-}Am)_{Chl}$ + $(Ms)_{Phg}$. (c) Pressure-temperature results from each of equilibrated illite-chlorite pair. (d) Comparison of the peak-metamorphic temperatures inferred from RSCM and the chlorite thermometry using the method by Vidal et al. (2006).

Figure 11. (a) Quartz with high fluid inclusion density from the Kodiak Landward Belt (Sample KO17H). (b) Quartz from higher-grade shear vein from the Kodiak Central Belt (Sample KO32F). Dashed lines represent trails of secondary fluid inclusions. (c) Two types of coexisting fluid inclusions in lower-grade veins: One-phase CH_4 and two-phase H_2O-rich with CH_4-CO_2 vapor bubble (Kodiak Landward Belt, sample KO17H). (d) two-phase H_2O rich fluid inclusions from quartz vein in the Kodiak Central Belt. Vapor bubble is composed of CO_2.

Figure 12. Box plots of estimated salinities of primary fluid inclusions and to a lesser extent of secondary inclusions in all the studied samples. Points next to each box plot correspond to the salinity of individual fluid inclusions in a given sample.

Figure 13. (a) Relative proportions of Na_2O, MgO, CaO, K_2O, FeO, SO_2 and Cl in evaporate mounds from decrepitated fluid inclusions. Each line represents the average composition from 3-10 points analyses acquired by EPMA in individual evaporate mounds. (b) Ca/Na vs. K/Na binary diagram and (c) Ca/Na vs. SO_2/Cl binary diagram of each individual point analysis in all examined evaporate mounds.

Figure 14. (a) The chlorite / (smectite + illite + muscovite) ratios based on XRD results. Note that for both localities there is an increase of the proportion of chlorite as a function of temperature. (b) Box plots of fluid inclusion salinities in quartz veins from this study as well as from previous studies concerning salinity in the Kodiak accretionary complex and the Shimanto Belt in Japan. Compilation of literature: Big Waterfall mélange, Kodiak (Rowe et al., 2009); Kodiak Formation, Alaska: pink – Afognak transect, red – Kodiak transect (Brantley & Fisher, 1997); Mugi mélange (Sakaguchi, 1999); Makimine mélange (Nishiyama et al., 2021).

Figure S1. X-ray diffraction patterns of samples from the Kodiak Formation (Alaska), the Foliated Morotsuka, and the Hyuga Tectonic Mélange (Japan).

Figure S2. SEM-EDS maps of evaporate mounds after the decrepitation method in (a) lower-grade quartz vein (Sample NOB_11C) and (b) higher-grade quartz vein (Sample KO30D).

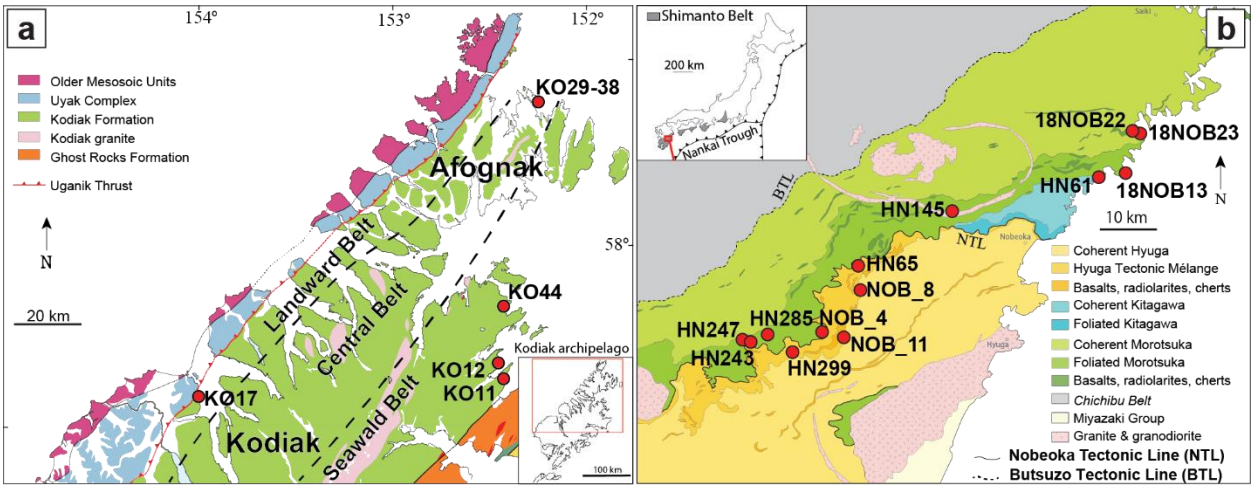

Figure 1.

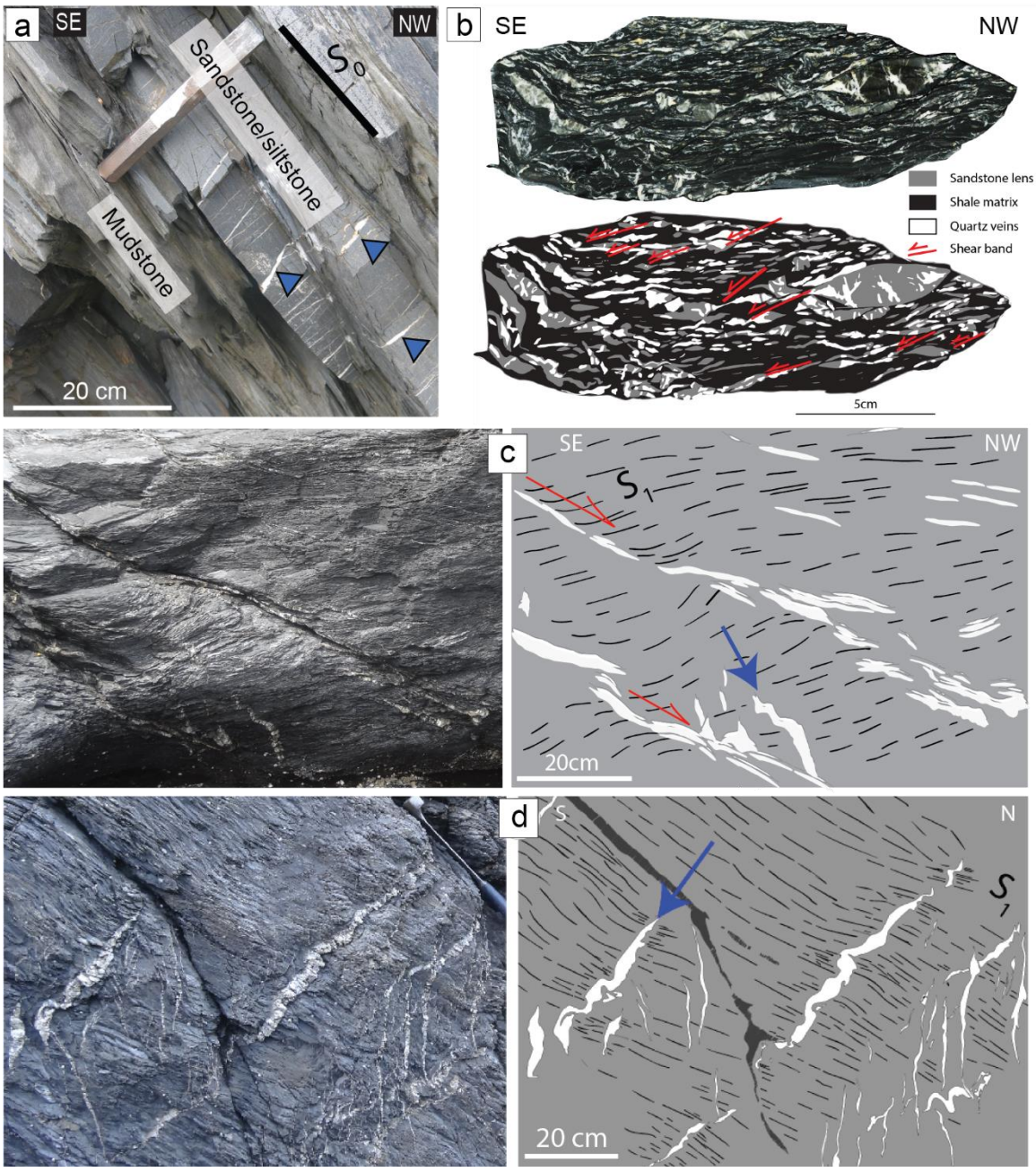

1213

1214 Figure 2.

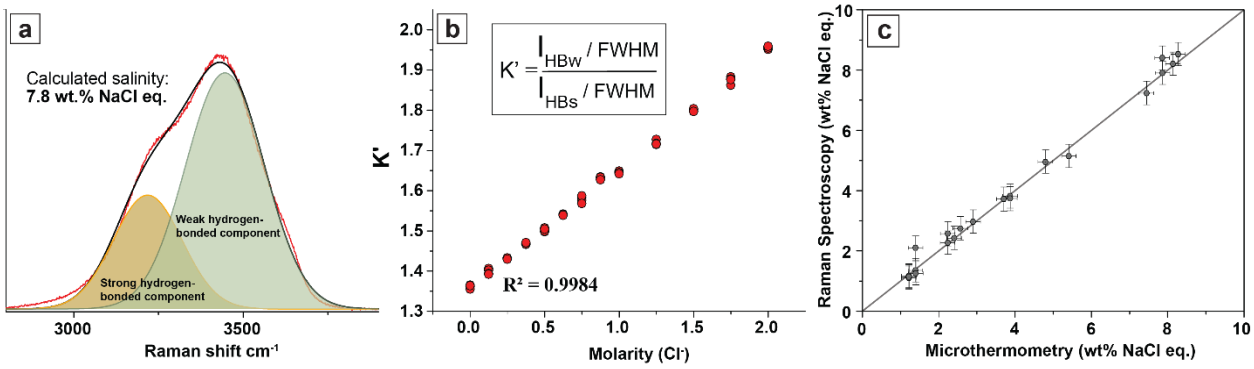

1215

1216 Figure 3.

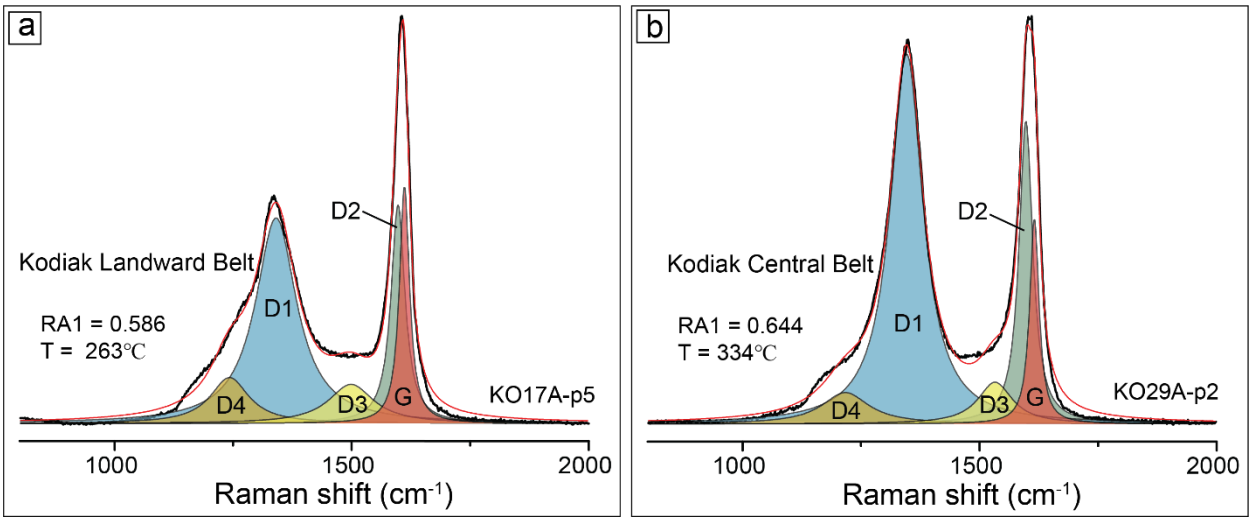

1217

1218 Figure 4.

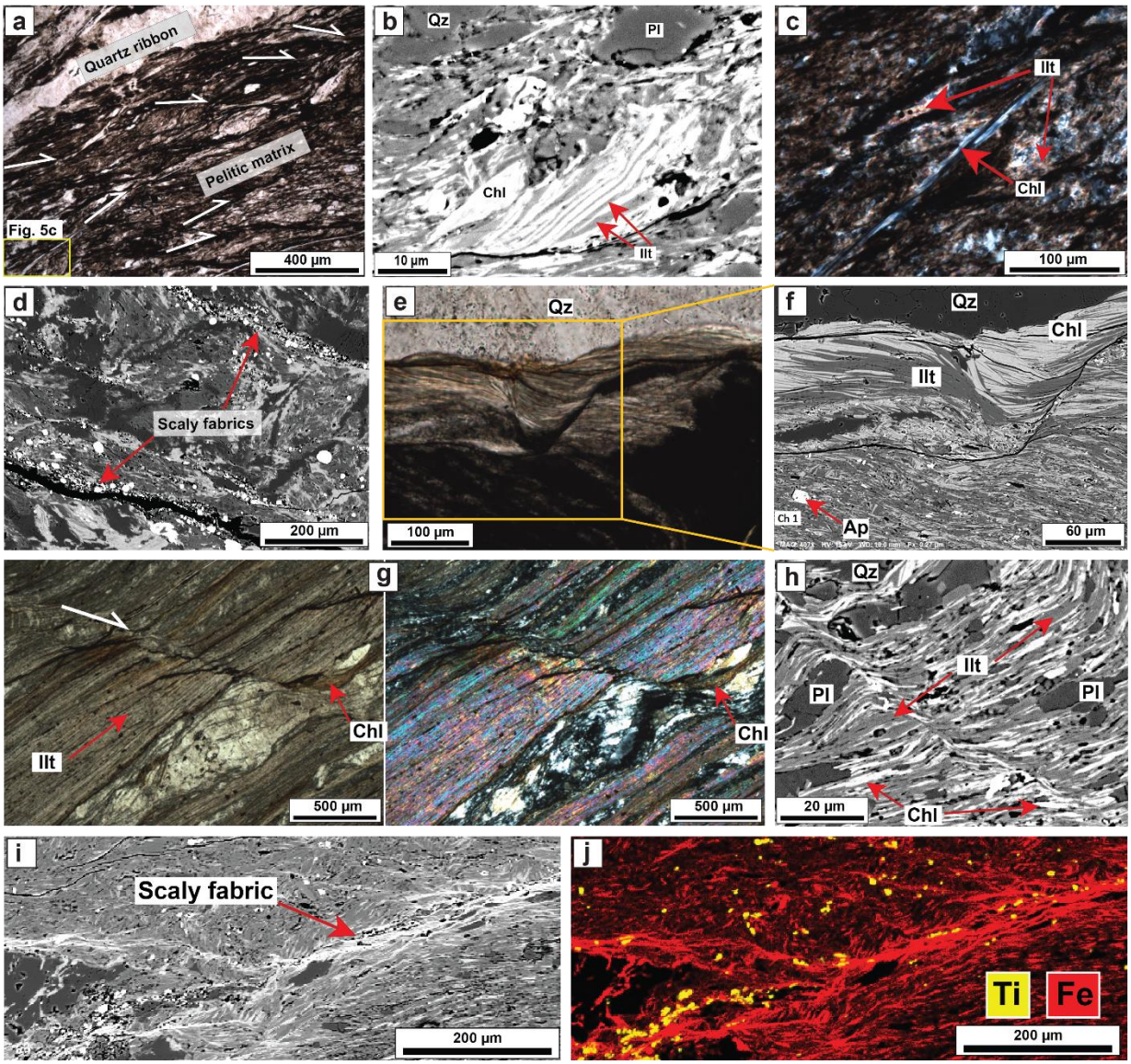

1219

1220 Figure 5.

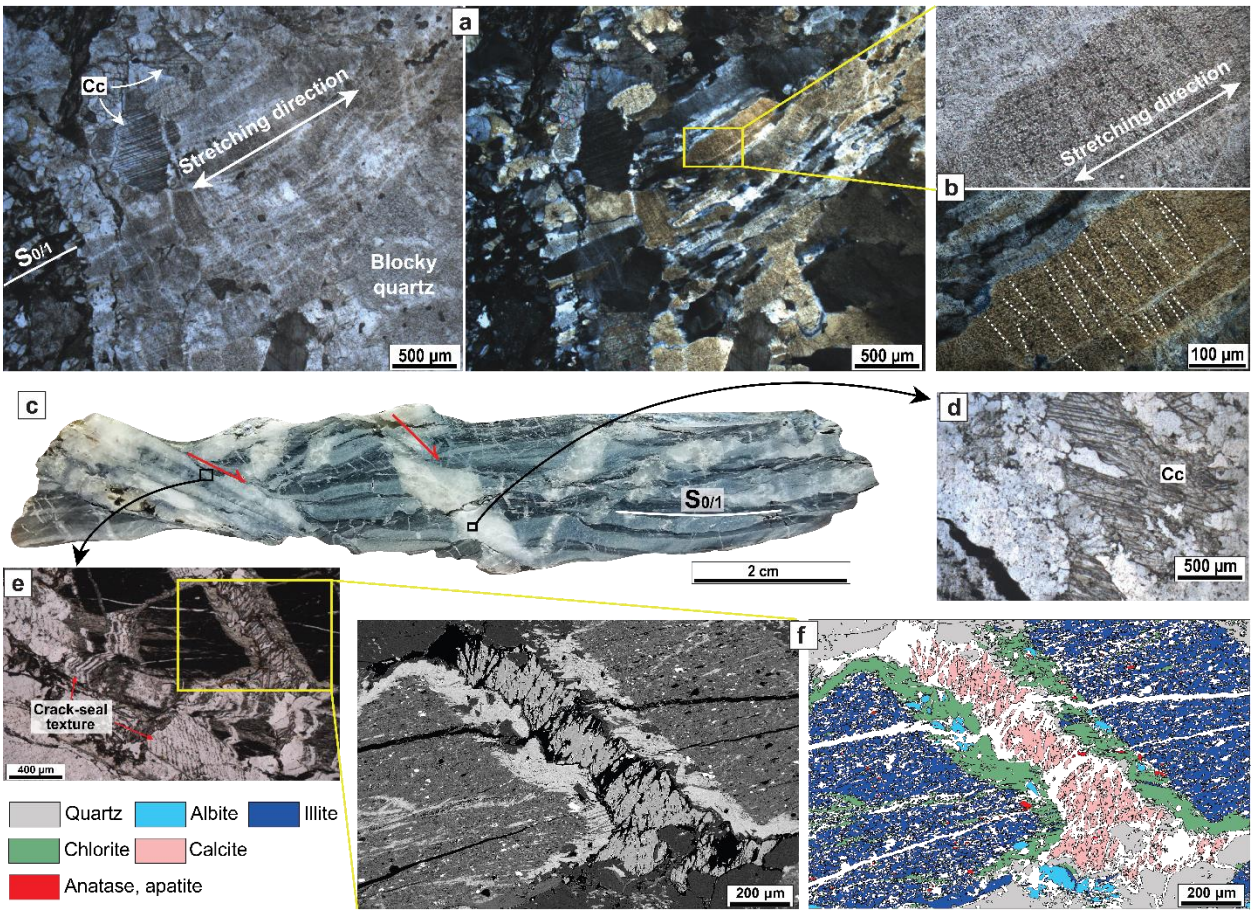

1221

1222 Figure 6.

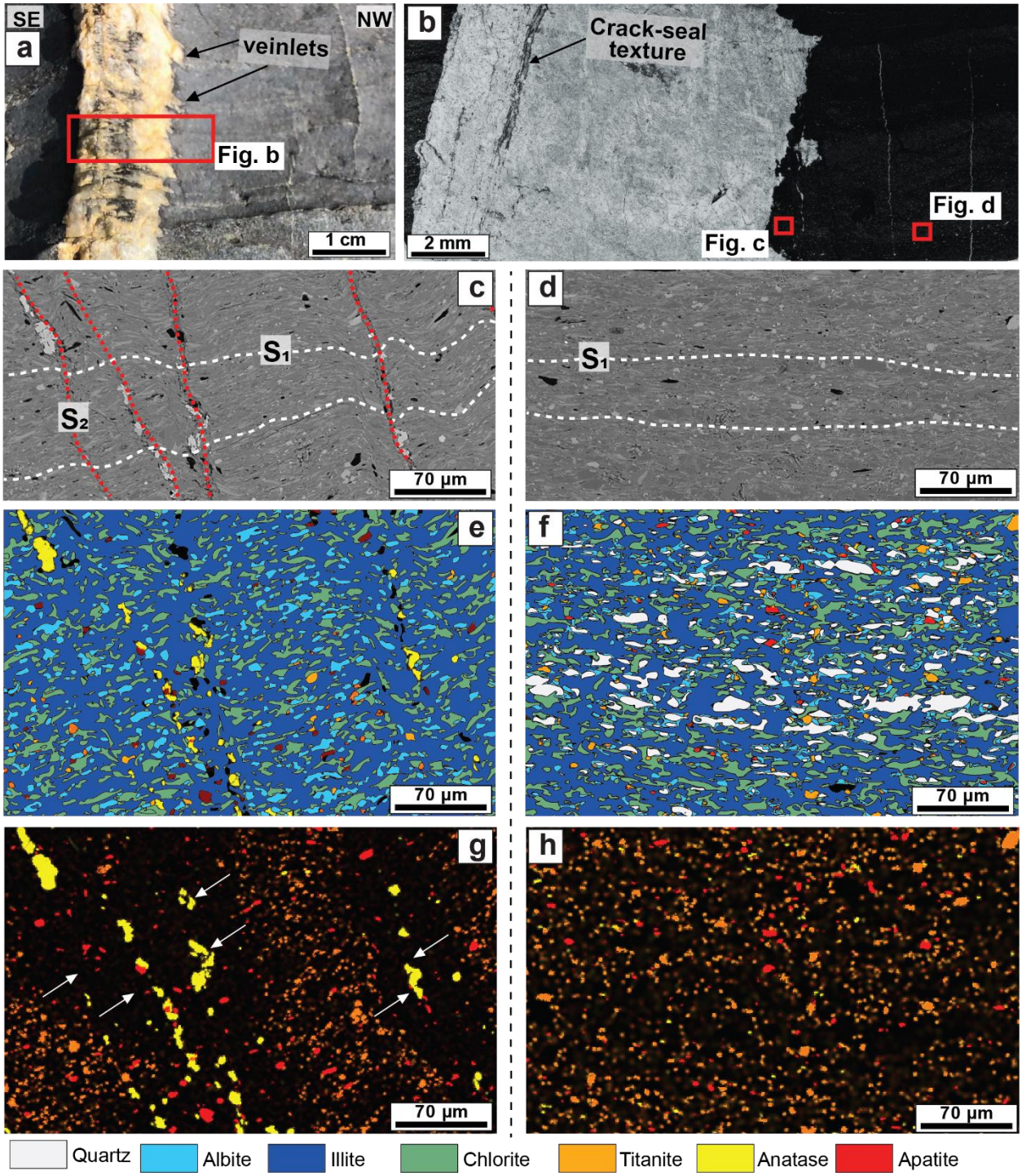

1223

1224 Figure 7.

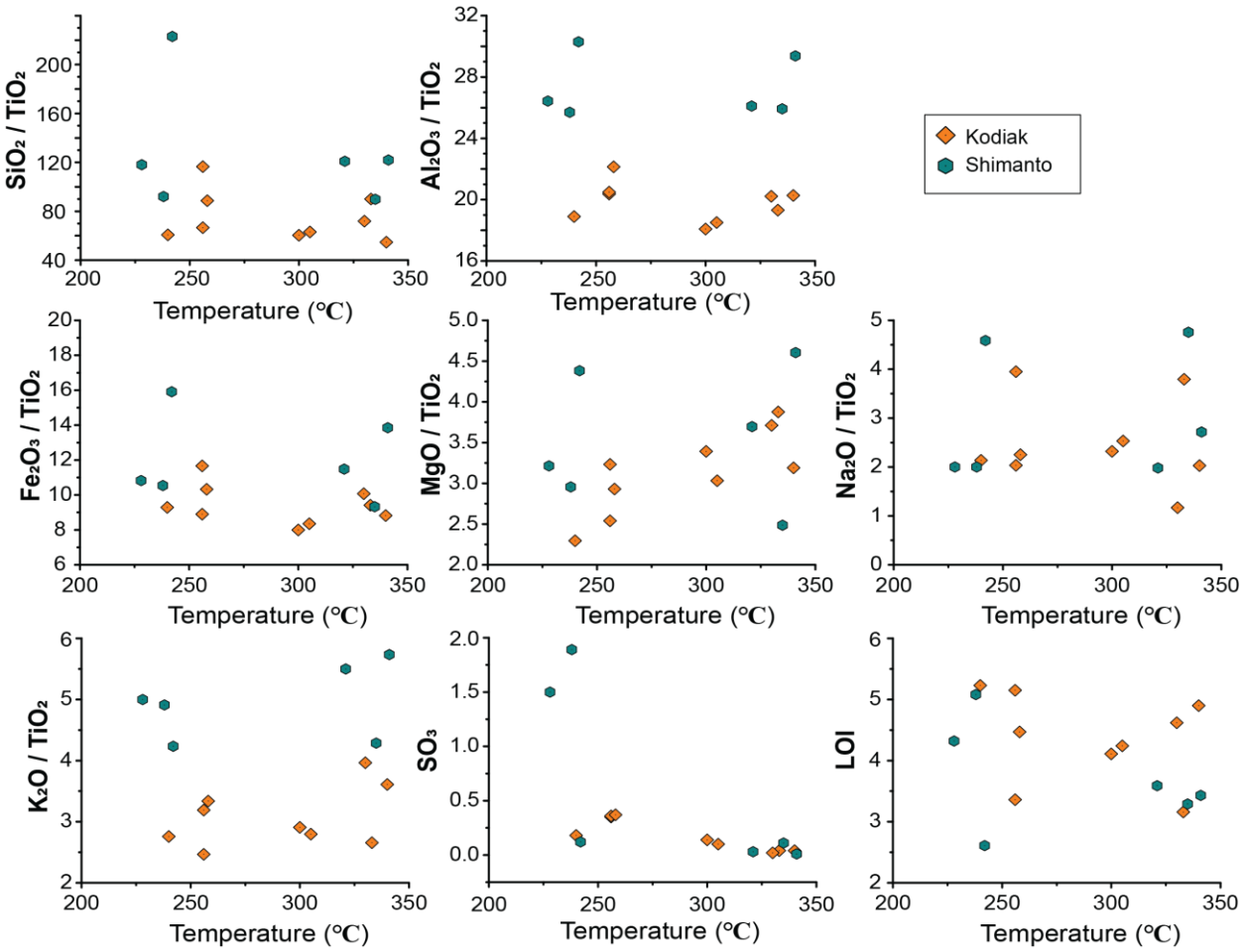

1225

1226 Figure 8.

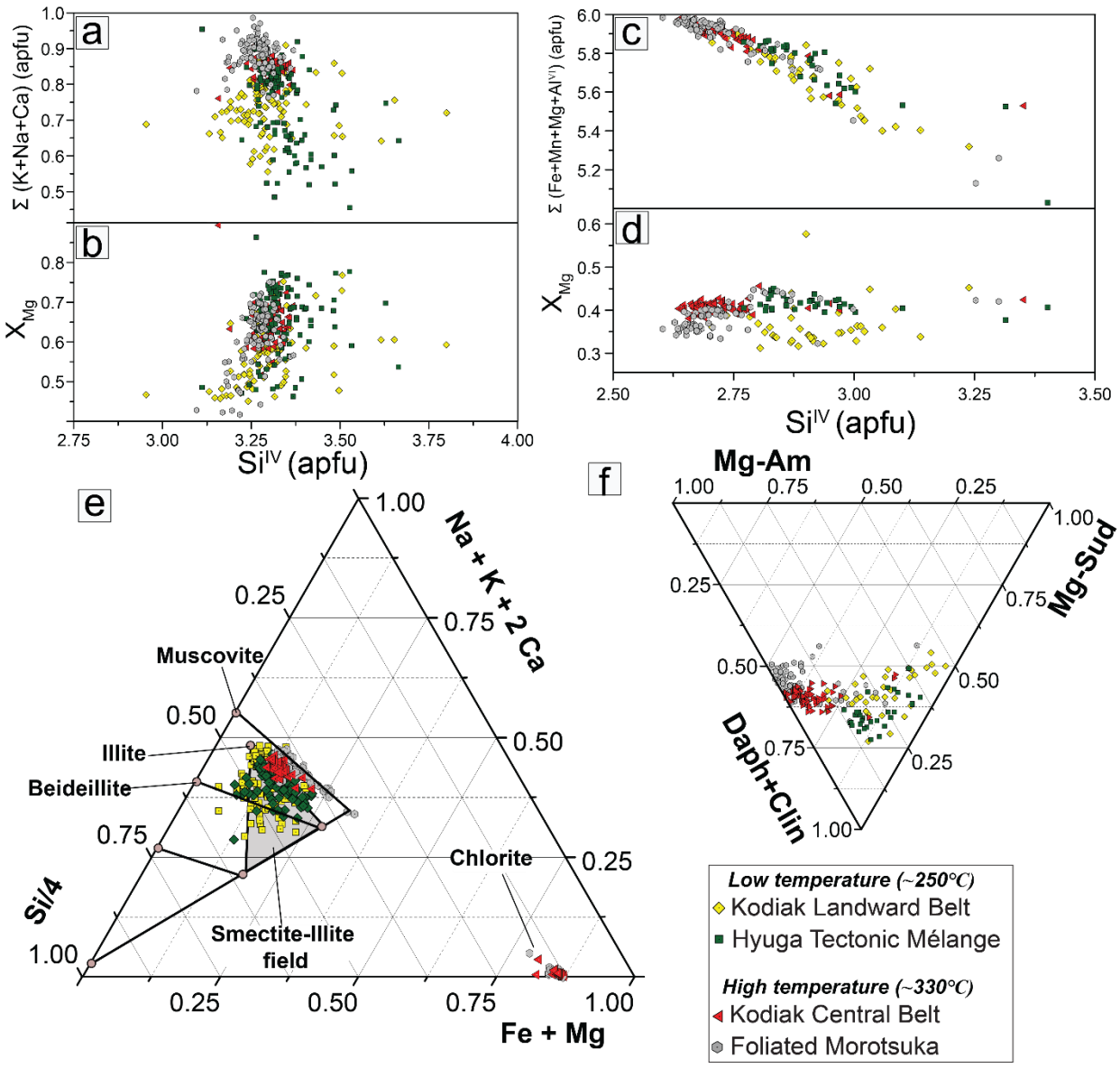

1227

1228 Figure 9.

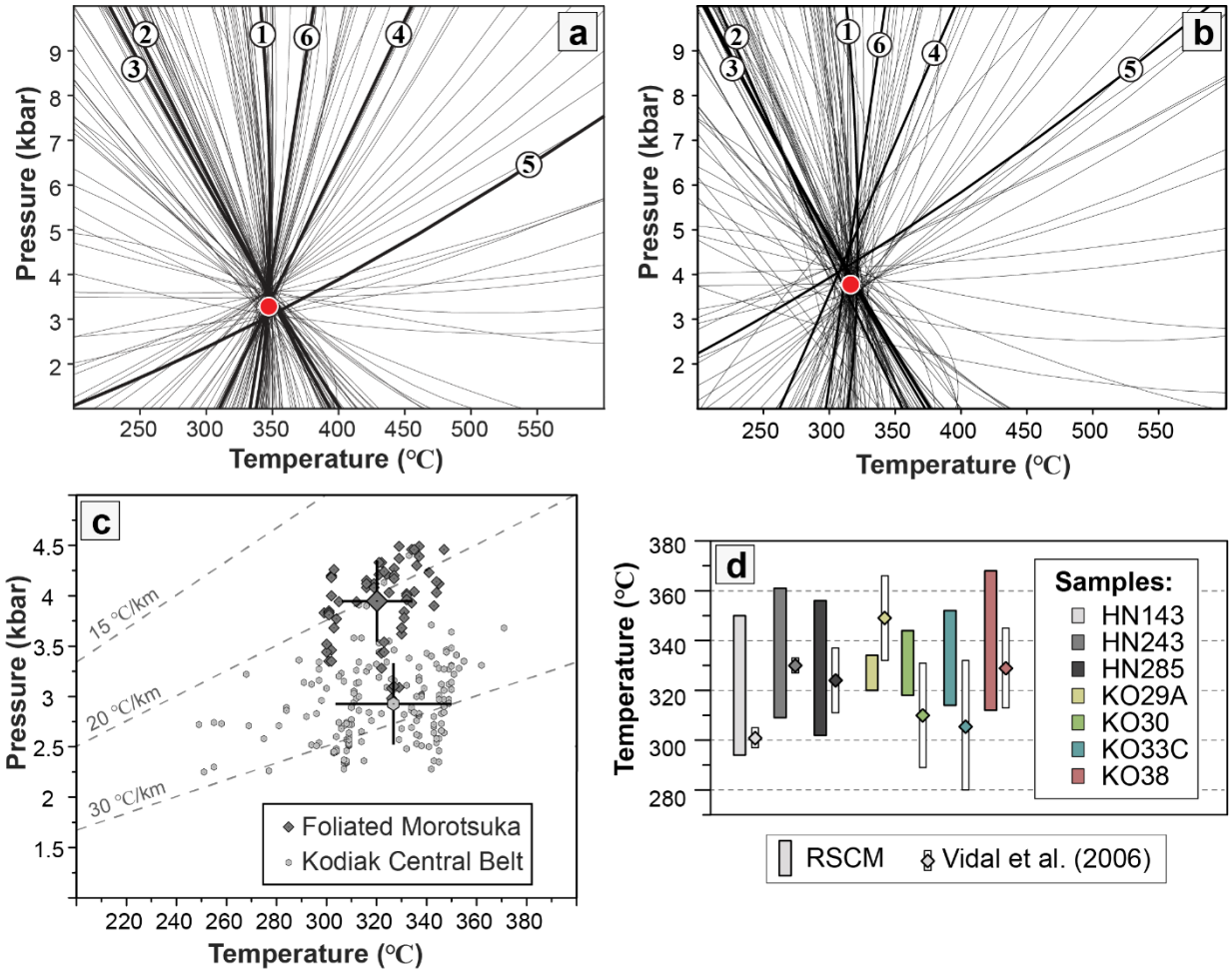

1229

1230 Figure 10.

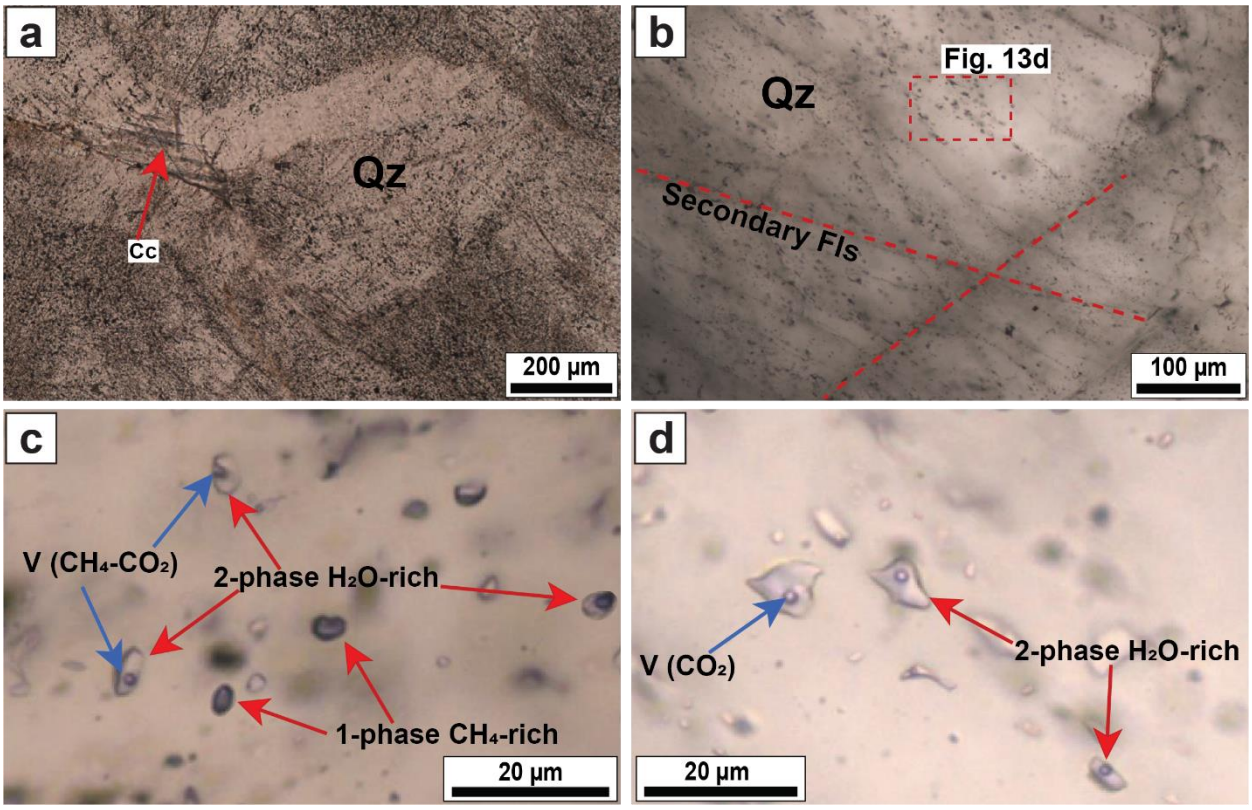

1231

1232 Figure 11.

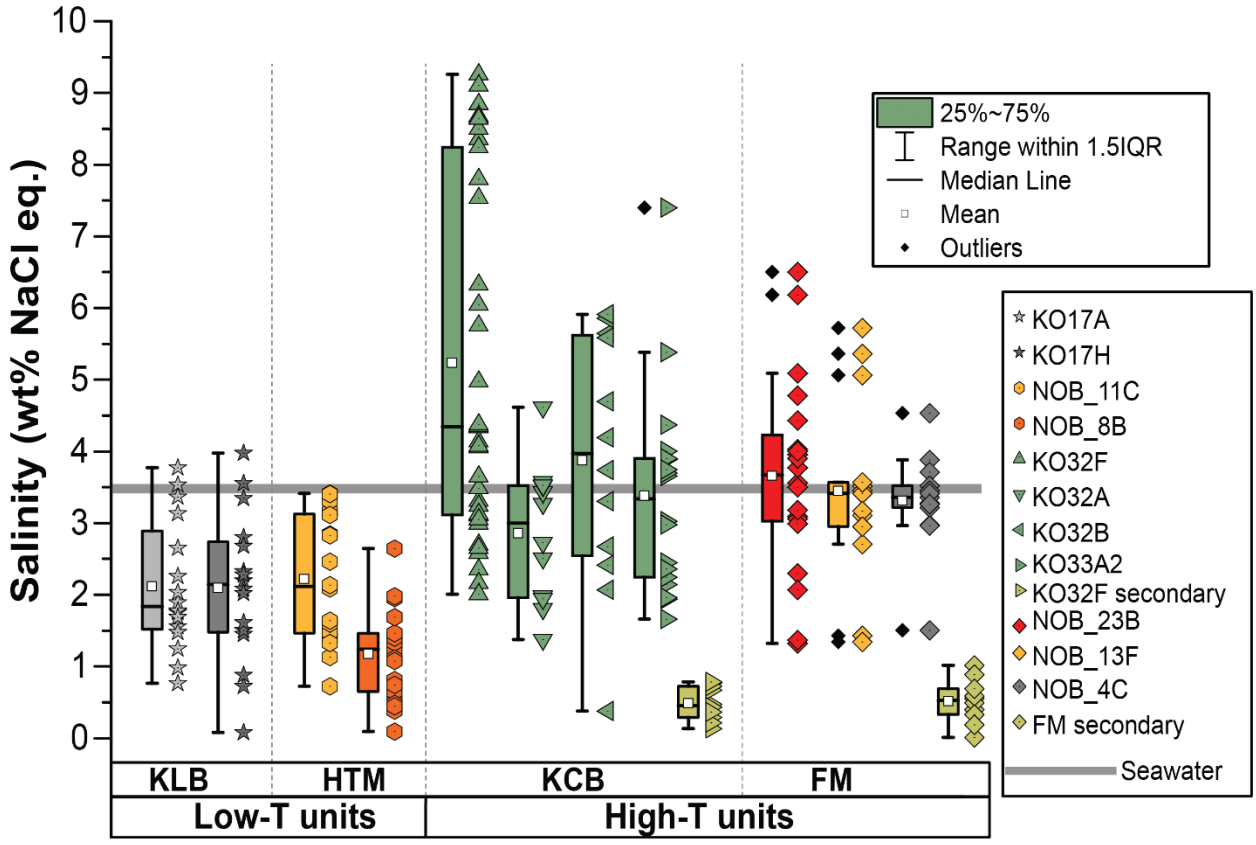

1233

1234 Figure 12.

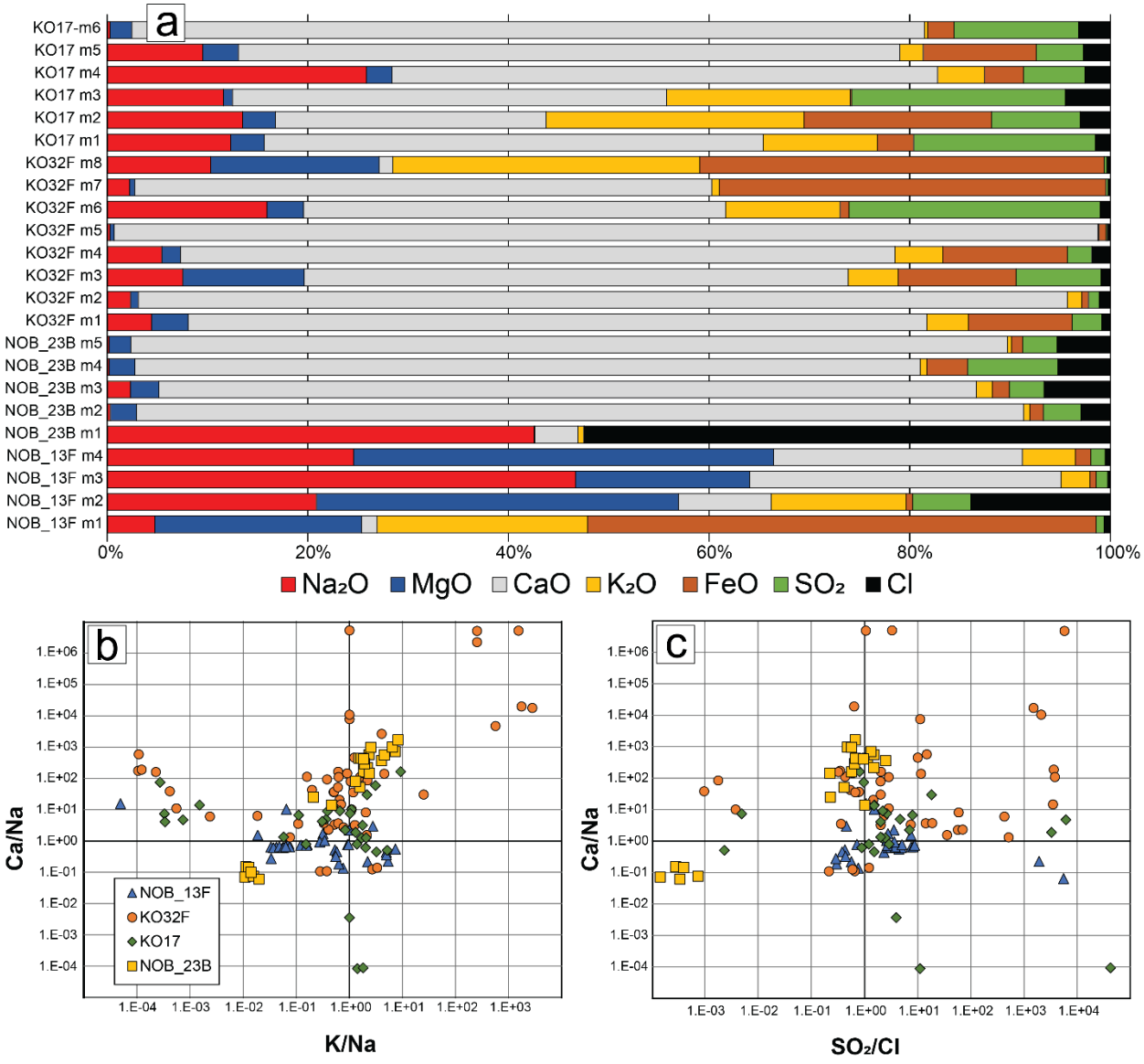

1235

1236 Figure 13.

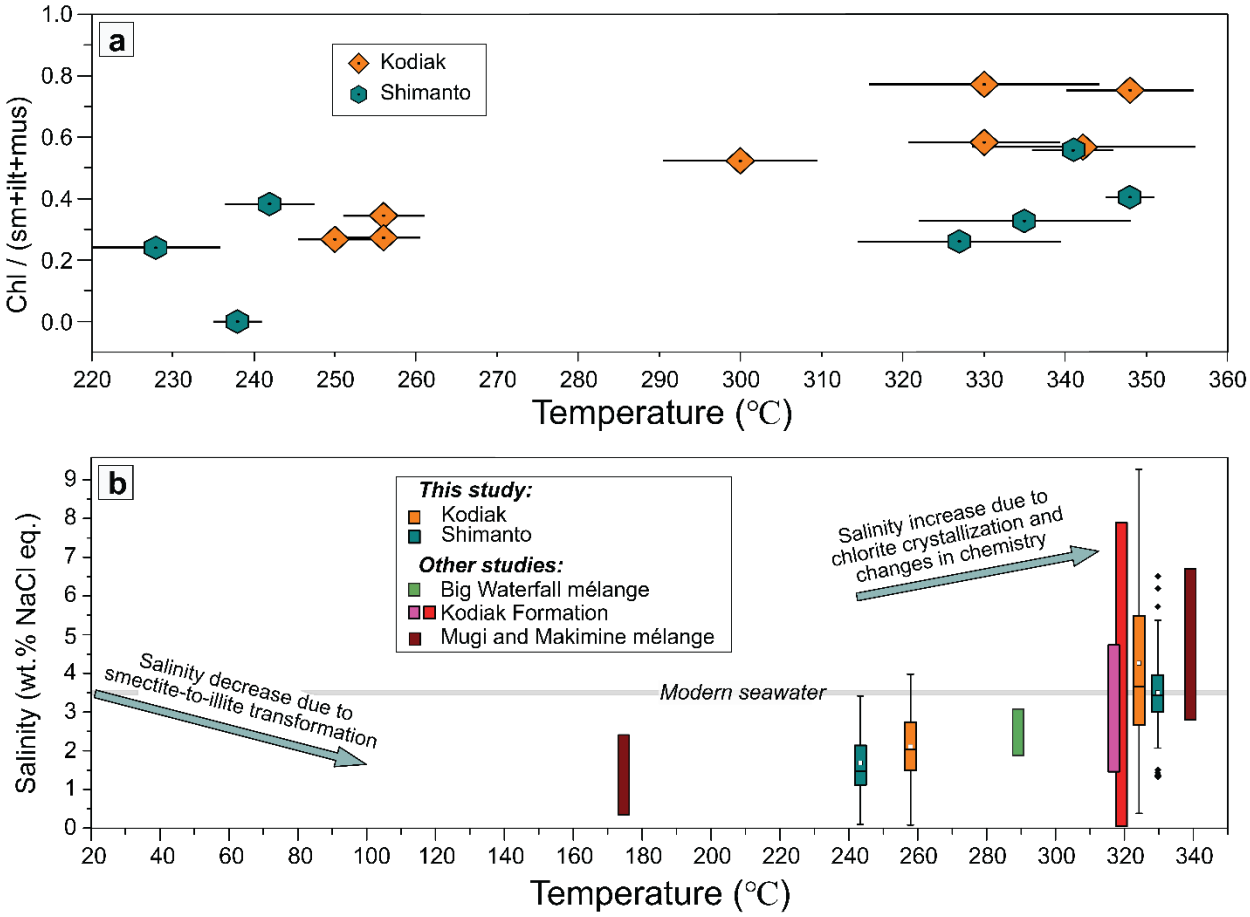

1237

1238 Figure 14.

1239 **TABLES**

1240 Table 1. Sample locations and pressure-temperature estimates based on Raman Spectroscopy of
1241 Carbonaceous Material and multi-phase equilibrium model. Literature references: [1]Palazzin et al. (2016);
1242 [2]Raimbourg et al. (2018); [3]Raimbourg et al. (2021).

	Sample	Longitude	Latitude	RSCM		Multi-phase equilibrium				Ref.
Kodiak				T (°C)	SD	T (°C)	SD	P (kbar)	SD	
Landward Belt	KO17A	-153.9843	57.6094	**251**	09					This study
	KO17B	-153.9843	57.5093	**256**	10					This study
	KO17E	-153.9841	57.6119	**240**	09					This study
Central Belt	KO29A	-152.218	58.3774	**327**	07	**349**	17	**3.5**	0.8	This study
	KO30	-152.2228	58.3542	**331**	13	**310**	21	**3.1**	0.4	This study
	KO32A	-152.245	58.3893	**330**	16					This study
	KO32F	-152.245	58.3893	**330**	16					This study
	KO33C	-152.2568	58.3576	**333**	19	**306**	26	**2.9**	0.3	This study
	KO36A	-152.2586	58.3661	**330**	29					This study

	KO38	-152.2865	58.3889	**340**	28	**329**	16	**3.0**	0.4	This study
Seaward Belt	KO11	-152.4386	57.6516	**300**	19					This study
	KO12B	-152.4764	57.6875	**348**	28					This study
	KO45C	-152.4385	57.8393	**344**	16					This study
Shimanto Belt										
Hyuga Tectonic Mélange	HN65	131.4036	32.5452	**240**	06					[1]
	HN85	131.3148	32.4287	**242**	11					This study
	HN299	131.279	32.4033	**228**	16					This study
Foliated Morotsuka	18NOB13	131.5433	32.7211	**323**	19					This study
	18NOB22A	131.8556	32.7552	**349**	06					This study
	18NOB23	131.8786	32.7614	**338**	10					[3]
	HN61	131.8559	32.7202	**348**	06					[2]
	HN143	131.5583	32.6137	**322**	28	**301**	04	**3.9**	0.3	This study
	HN243	131.2075	32.4094	**335**	26	**330**	03	**3.7**	0.4	This study
	HN247	131.2026	32.3095	**327**	33					This study
	HN285	131.2392	32.4200	**329**	27	**324**	13	**4**	0.4	This study [1]

Table 2. Major element compositions of metapelites expressed in wt.% from the Kodiak accretionary complex and the Shimanto Belt of Japan.

	Kodiak Landward Belt				**Central Belt**			**Seaward Belt**		**Hyuga Tectonic Mélange**			**Foliated Morotsuka**		
Sample	**KO17B**	**KO17C**	**KO17D**	**KO17E**	**KO33A**	**KO36A**	**KO38**	**KO11C**	**KO43C**	**HN64**	**HN85**	**HN299**	**NOB_23B**	**HN145**	**HN243**
SiO_2	69.9	59.23	62.98	57.67	65.7	59.69	54.76	58.53	59.32	61.72	75.83	66.14	64.65	67.69	62.89
TiO_2	0.60	0.89	0.71	0.95	0.73	0.83	1.00	0.97	0.94	0.67	0.34	0.56	0.53	0.56	0.70
Al_2O_3	12.22	18.24	15.72	17.95	14.1	16.78	20.27	17.54	17.40	17.22	10.3	14.80	15.57	14.62	18.15
Cr_2O_3	0.04	0.02	0.02	0.02	0.02	0.02	0.03	0.03	0.03	0.01	0.01	0.02	0.02	0.02	0.01
Fe_2O_3	7.00	7.92	7.33	8.82	6.87	8.36	8.82	7.76	7.85	7.06	5.41	6.06	7.34	6.43	6.53
MnO	0.04	0.08	0.10	0.12	0.09	0.11	0.11	0.10	0.13	0.07	0.15	0.07	0.35	0.08	0.13
MgO	1.94	2.26	2.08	2.18	2.83	3.08	3.19	3.29	2.85	1.98	1.49	1.80	2.44	2.07	1.74
CaO	0.33	0.79	0.88	1.20	1.00	0.96	0.99	1.28	1.18	0.74	0.62	0.88	0.86	0.06	0.07
Na_2O	2.37	1.81	1.60	2.03	2.77	0.97	2.03	2.25	2.38	1.34	1.56	1.12	1.44	1.11	3.33
K_2O	1.48	2.84	2.37	2.62	1.94	3.29	3.61	2.82	2.63	3.29	1.44	2.80	3.04	3.08	3.00
P_2O_5	0.16	0.26	0.22	0.28	0.22	0.25	0.27	0.44	0.36	0.10	0.08	0.09	0.09	0.07	0.11
SO_3	0.35	0.36	0.37	0.18	0.04	0.02	0.04	0.14	0.10	1.89	0.12	1.50	0.01	0.03	0.11
SrO	0.02	0.02	0.02	0.02	0.03	0.02	0.01	0.02	0.03	0.02	0.01	0.02	0.02	0.01	0.01
BaO	0.05	0.11	0.08	0.10	0.12	0.14	0.15	0.11	0.12	0.07	0.03	0.06	0.05	0.06	0.06
LOI	3.36	5.15	4.47	5.23	3.16	4.62	4.90	4.11	4.24	5.08	2.61	4.32	3.43	3.59	3.29
Total	99.96	100.1	99.05	99.53	99.72	99.24	100.3	99.51	99.7	101.35	100.05	100.35	99.97	99.59	100.20

Table 3. Mineral phase proportions based on X-Ray Diffraction patters using the Rietveld method (Rietveld, 1969). I/S stands for smectite-illite mixed layers.

Formation	Landward Belt			Central Belt			Seaward Belt		HTM			Foliated Morotsuka			
Sample	KO17B	KO17C	KO17E	KO33A	KO36A	KO38	KO45C	KO11C	HN299	HN64	HN85	23B	61	HN243	HN246
Major phases															
Illite/muscovite	23.2	42.1	47.6	21	40.7	42.4	25.5	36.5	42.4	39.3	36.4	38.6	38.1	31.1	31.2
Chlorite	8.0	11.5	12.7	16.2	23.7	24.1	19.2	19.1	10.2	0.0	13.9	21.6	15.4	10.2	8.1
I/S	1.8	2.6	4.0	0.0	0.0	0.0	0.0	0.0	4.5	2.3	1.4	0.9	0.0	0.0	0.0
Quartz	43.1	27	17.3	34.2	25.7	15.8	29.4	22.7	27.7	32.9	35.1	23.9	25.2	30	30.0
Plagioclase	19.5	13.1	16.2	25.2	5.2	16.0	22.2	17.7	10.1	13.3	12.6	11.5	20.2	26.3	26
K feldspar	0.0	0.0	0.0	3.3	4.7	1.7	2.4	3.8	0.0	0.0	0.0	2.4	0.0	2.3	2.2
Phyllosilicates	33	56.2	64.3	37.2	64.4	66.5	44.7	55.6	57.1	41.6	51.7	61.1	53.5	41.3	39.3
Chl / (Chl+mus)	24.2	20.5	19.8	43.5	36.8	36.2	43.0	34.4	17.9	0.0	26.9	35.4	28.8	24.7	20.6
I/S / phs	5.5	4.6	6.2	0.0	0.0	0.0	0.0	0.0	7.9	5.5	2.7	1.5	0.0	0.0	0.0
Accessory phases															
Calcite	0.9		0.6				1.2		0.5	<0.5	< 0.5	0.9			
Magnesite													0.8		
Serpentine	3.4	2.8							1.6					1.8	
Pyrite	< 0.5	0.9	< 0.5	<0.5	<0.5	<0.5	<0.5	<0.5	1.5	0.9	< 0.5			< 0.5	< 0.5
Dolomite									1.1	1					
Siderite										6.1					
Kaolinite										4					

1249

1250

1251

1252